

# Colors and patterns of black hole X-ray binary GX 339–4

Iliia A. Kosenkov<sup>1,2</sup>, Alexandra Veledina<sup>1,3,4</sup>, Valery F. Suleimanov<sup>4,5,6</sup>, and Juri Poutanen<sup>1,3,4</sup>

<sup>1</sup> Department of Physics and Astronomy, FI-20014 University of Turku, Finland

<sup>2</sup> Department of Astrophysics, St. Petersburg State University, Universitetskiy pr. 28, Peterhof, 198504 St. Petersburg, Russia

<sup>3</sup> Nordita, KTH Royal Institute of Technology and Stockholm University, Roslagstullsbacken 23, SE-10691 Stockholm, Sweden

<sup>4</sup> Space Research Institute of the Russian Academy of Sciences, Profsoyuznaya Str. 84/32, 117997 Moscow, Russia

<sup>5</sup> Institut für Astronomie und Astrophysik, Kepler Center for Astro and Particle Physics, Universität Tübingen, Sand 1, 72076 Tübingen, Germany

<sup>6</sup> Kazan (Volga region) Federal University, Kremlevskaya str. 18, Kazan 420008, Russia

## ABSTRACT

Black hole X-ray binaries show signs of non-thermal emission in the optical/near-infrared range. We analyze the optical/near-infrared SMARTS data on GX 339–4 over the 2002–2011 period. Using the soft state data, we estimate the interstellar extinction towards the source and characteristic color temperatures of the accretion disk. We show that various spectral states of regular outbursts occupy similar regions on the color-magnitude diagrams, and that transitions between the states proceed along the same tracks despite substantial differences in the observed light curves morphology. We determine the typical duration of the hard-to-soft and soft-to-hard state transitions and the hard state at the decaying stage of the outburst to be one, two and four weeks, respectively. We find that the failed outbursts cannot be easily distinguished from the regular ones at their early stages, but if the source reaches 16 mag in V-band, it will transit to the soft state. By subtracting the contribution of the accretion disk, we obtain the spectra of the non-thermal component, which have constant, nearly flat shape during the transitions between the hard and soft states. In contrast to the slowly evolving non-thermal component seen at optical and near-infrared wavelengths, the mid-infrared spectrum is strongly variable on short timescales and sometimes shows a prominent excess with a cutoff below  $10^{14}$  Hz. We show that the radio to optical spectrum can be modeled using three components corresponding to the jet, hot flow and irradiated accretion disk.

**Key words.** accretion, accretion disks – black hole physics – methods: data analysis – stars: black holes – stars: individual: GX 339–4 – X-rays: binaries

## 1. Introduction

GX 339–4 is a well-studied black hole (BH) low-mass X-ray binary (LMXB) that was discovered as a bright and variable X-ray source using MIT *OSO-7* experiment (Markert et al. 1973). The source is known to undergo recurrent outbursts every 2–3 years and it became a standard target for multiwavelength campaigns (Homan et al. 2005; Belloni et al. 2005, 2006; Tomsick et al. 2008; Shidatsu et al. 2011; Cadolle Bel et al. 2011; Motta et al. 2011; Rahoui et al. 2012; Buxton et al. 2012; Corbel et al. 2013b). During outbursts the source undergoes a transition between different states that can be distinguished using a variety of criteria, including the X-ray hardness ratio, quasi-periodic oscillations and other timing properties (Homan & Belloni 2005; McClintock & Remillard 2006; Remillard & McClintock 2006; Belloni 2010).

The origin of these states is still not very well understood, but is generally associated with the changes in the accretion flow geometry (see, e.g., Esin et al. 1997; Poutanen et al. 1997; Zdziarski et al. 2004; Done et al. 2007). In the soft X-ray state, the spectrum consists of a thermal component associated with the standard cold accretion disk (Shakura & Sunyaev 1973) and an additional power-law-like tail from the non-thermal corona (Poutanen & Coppi 1998; Gierliński et al. 1999; Zdziarski et al. 2001). In the hard state, the emission from the cold disk is greatly reduced due to its truncation at a radius significantly larger than the radius of the innermost stable orbit; the emission instead is dominated by thermal Comptonization of some seed photons

(cold disk and internal synchrotron) in an inner hot, geometrically thick accretion flow. The transitions between the spectral states happen due to a change in the truncation radius, which results in a variation of the relative contributions of the cold disk and the hot flow and also lead to corresponding changes in the timing properties (Done et al. 2007; Gilfanov 2010; Poutanen & Veledina 2014; De Marco et al. 2015; Stiele & Kong 2017; Poutanen et al. 2018; Mahmoud et al. 2019).

For many years it was obvious that the X-ray emitting region of accreting BHs is rather compact because of the observed fast variability. On the other hand, the optical/near-infrared (ONIR) emission was thought to originate mostly from the outer disk irradiated by the central X-ray source. The first evidence that the situation is not so simple came already in the beginning of 1980s, when the fast optical variability and quasi-periodic oscillations at 20 s were detected from GX 339–4 by Motch et al. (1982), which were interpreted as a signature of emission from the hot accretion flow or corona (Fabian et al. 1982). Soon after, Motch et al. (1983) carried out simultaneous optical/X-ray observations which demonstrated a complicated structure of the cross-correlation function (CCF) with a precognition dip. Recently, similar CCFs were found in three BHs: XTE J1118+480 (Kanbach et al. 2001; Hynes et al. 2003a), Swift J1753.5–0127 (Durant et al. 2008, 2009, 2011; Hynes et al. 2009) and in GX 339–4 (Gandhi et al. 2008, 2010). The shape of the CCF can be explained if the optical emission contains two components: synchrotron emission from the hot flow and the reprocessed radiation that are anti-correlated and correlated with the

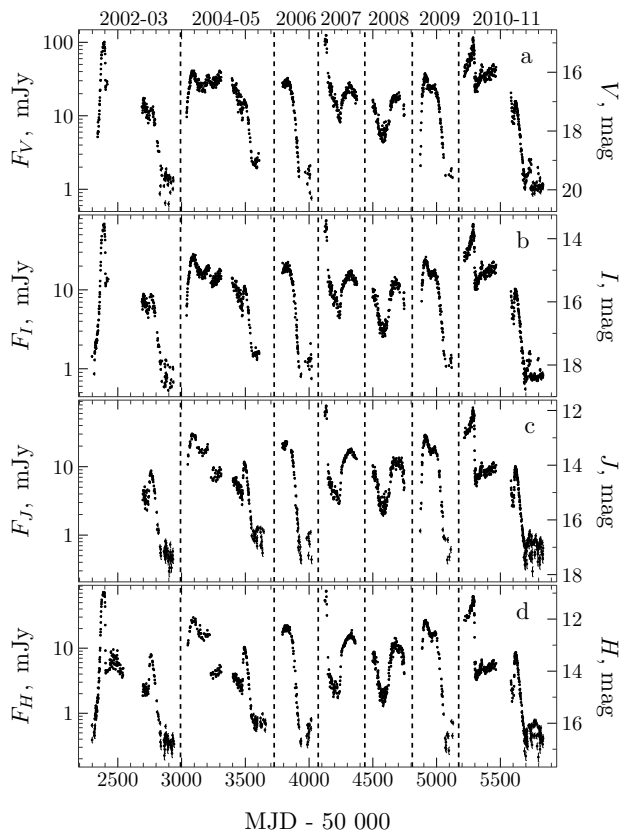


**Fig. 1.** Observed ONIR magnitudes and corrected for the interstellar extinction fluxes of GX 339–4 in four ONIR filters (*V*, *I*, *J* and *H*). Vertical dashed lines separate data into 7 intervals corresponding to each of the regular/failed outbursts.

X-rays, respectively (Veledina et al. 2011). However, the shape of the CCF seems to be wavelength-dependent. For instance, the infrared/X-ray CCF of GX 339–4 showed a single peak with no precognition dip (Casella et al. 2010), which was successfully explained by a jet model, where the emission is powered by internal shocks (Malzac et al. 2018). Thus it is clear that the ONIR emission is not completely dominated by the accretion disk, but has at least one additional (non-thermal) component, either from the hot flow, or the jet, or both.

Signatures of this component are seen in the long-term variability as bright ONIR flares, which appear in the hard state (Hynes et al. 2000; Jain et al. 2001; Buxton & Bailyn 2004; Kalemci et al. 2013). Spectral evolution of the flare in XTE J1550–564 is consistent with the hot accretion flow scenario (Veledina et al. 2013; Poutanen & Veledina 2014). In Swift J1753.5–0127 the jet emission is known to be weak in radio and its contribution to the ONIR band is likely small (Durant et al. 2009), while the ONIR-X-ray broad-band spectra can well be explained by the hot flow model (Kajava et al. 2016). On the other hand, the soft ONIR spectra of 4U 1543–47 (Kalemci et al. 2005) and MAXI J1836–194 (Russell et al. 2013) argue in favor of the jet scenario.

The origin of this non-thermal component can give us a clue to understanding the nature of the accretion-ejection engine operating in the BH vicinity. This aim can be reached by studying the evolution of its spectral shape throughout the outburst and in particular during the transitions between the states. This requires measurements of the interstellar extinction and subtraction of

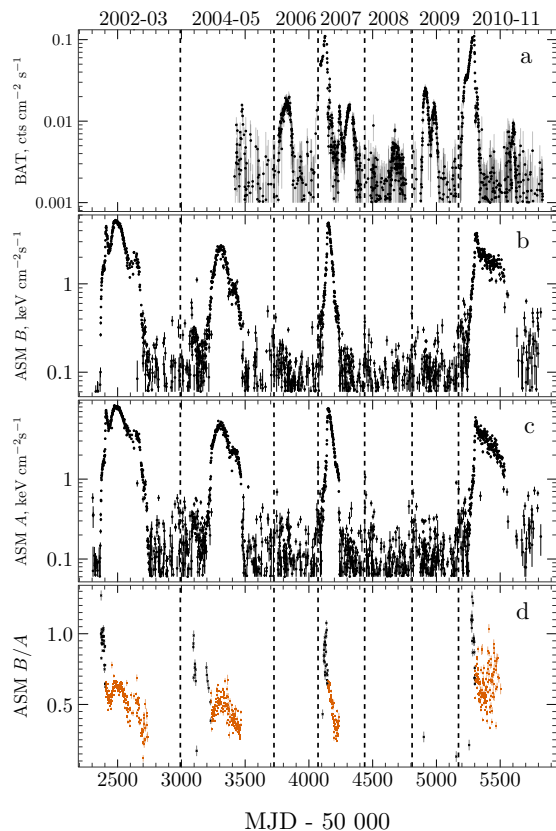


**Fig. 2.** X-ray light curves of GX 339–4: (a) *Swift*/BAT count rate in the 15–150 keV band, (b) ASM B (3–5 keV) flux, (c) ASM A (1.5–3 keV) light curve, (d) ASM B/A hardness ratio. Orange points correspond to the soft states selected using ONIR data from four outbursts. Errors are  $1\sigma$ .

the (irradiated) accretion disk contribution. From this perspective, GX 339–4 is an interesting source because it has served as a target for numerous multiwavelength campaigns. The aim of this work is to study the behavior of the source spectrum on the color-magnitude diagram (CMD) and the evolution of the non-thermal component using spectral decomposition.

The paper is structured as follows. In Sect. 2, we describe the data used for the analysis. Sect. 3 contains details of the analysis, determination of the interstellar extinction, comparison of different outbursts, and determination of the spectrum of the non-thermal component. In Sect. 4 we discuss the observed ONIR properties and their connection to the X-rays. We also discuss the origin of the non-thermal component in terms of the hot flow and jet models. We conclude in Sect. 5.

## 2. Data

Monitoring of GX 339–4 in the ONIR has been conducted using the ANDICAM camera (DePoy et al. 2003) on the Small and Moderate Aperture Research Telescope System (SMARTS; Subasavage et al. 2010).<sup>1</sup> We use the publicly available SMARTS data in *V*, *I*, *J* and *H* filters taken in 2002–2011 (Buxton et al. 2012).<sup>2</sup> We split the ONIR light curves into 7 intervals, each cov-

<sup>1</sup> <http://www.astro.yale.edu/smarts/xrb/home.php>

<sup>2</sup> The data mentioned with the original publication (Buxton et al. 2012) cover 2002–2010 period and the fluxes in *I* filter are computed using an incorrect extinction  $A_I$ .

**Table 1.** Descriptions of the outburst phases.

Outburst phase	Abbreviation	Description
Rising phase	RPh	The initial phase of the outburst, during which both X-ray and ONIR fluxes increase and the source becomes redder
Rising hard state	RHS	The period in the first ONIR flare, during the hard X-ray state, when the ONIR colors stabilize
Hard to soft transition	HtS	The short, about 5–10 d, transition to the soft state, over which the ONIR colors become bluer and X-ray spectra become softer
Soft state	SS	Period during the soft X-ray state when the ONIR spectra are dominated by the accretion disk emission
Soft to hard transition	StH	The short, about 10–20 d, period over which the ONIR colors become redder and the source departs from the soft X-ray state
Decaying hard state	DHS	The period within the second flare of about 20–30 d, when the ONIR colors are stable and red
Decaying phase	DPh	The period when ONIR fluxes decay towards the quiescence
Quiescence	Q	The period of low activity between the outbursts

**Table 2.** Start and end dates of the outbursts and start dates of each identified outburst phase (in MJD).

Years	Start	RPh	RHS	HtS	SS	StH	DHS	DPh	Q	End
Regular outbursts										
2002–2003	52298	52298	52374	52400	52405	52738	52756	52786	52834	52942
2004–2005	53040		53040	53221	53231	53473	53490	53513	53553	53661
2007	54124		54124	54137	54146	54236	54252			54376
2010–2011	55217		55217	55295	55302	55602	55613	55645	55689	55836
Failed outbursts										
2006	53792						53792	53867	53935	54020
2008	54498		54498				54634			54747
2009	54872	54872	54885				54953	55000	55083	55129

**Notes.** Phase definitions are described in Table 1 and Section 3.1.

ering one of the regular or failed outbursts (see Sect. 3.1). The light curves, corrected for interstellar extinction (see Sect. 3.2), are shown in Fig. 1.

The X-ray data are taken from the *Rossi X-ray Timing Explorer* All-Sky Monitor (ASM)<sup>3</sup> (Bradt et al. 1993), which provides observations of GX 339–4 in three energy ranges (1.5–3, 3–5 and 5–12 keV). The count rates from different channels are converted to the observed fluxes using an empirical linear relation of Zdziarski et al. (2002). We also make use of the *Neil Gehrels Swift Observatory* Burst Alert Telescope (*Swift*/BAT)<sup>4</sup> (Gehrels et al. 2004; Barthelmy et al. 2005), which operates in the 15–150 keV range. The BAT, ASMA and B light curves as well as the ASMB/A hardness ratio are shown in Fig. 2.

The mid-infrared (mid-IR) data, obtained by the *Wide-field Infrared Survey Explorer* satellite (*WISE*, Wright et al. 2010), are adopted from Gandhi et al. (2011). All reported 13 observations of GX 339–4 are taken during 24 hours on MJD 55265.88–55266.88, i.e. within half a day from the SMARTS observation on MJD 55266.36 (Buxton et al. 2012). The mid-IR data are corrected for the interstellar extinction (see section 2.2.3 in Gandhi et al. 2011).

We also use the radio data obtained by the Australian Telescope Compact Array (ATCA, Wilson et al. 2011) in 5.5 and 9 GHz bands. Out of two closest to the SMARTS/*WISE* quasi-simultaneous spectrum observations (MJD 55262.91 and 55269.80, see table 1 in Corbel et al. 2013b)

we select the second one, which has a positive slope in the radio and can be extrapolated to the mid-IR *WISE* data.

### 3. Light curve analysis and results

#### 3.1. Outburst phase separation

We use ONIR light curves to split regular outbursts, when GX 339–4 reaches the soft state, into different phases: rising phase (RPh), hard state at the rising stage (RHS), transition from the hard to the soft state (HtS), soft state (SS), transition from the soft to the hard state (StH), hard state at the decaying stage (DHS), decaying phase (DPh) and quiescence (Q), see Table 1. Different states are first roughly identified using the X-ray data, as in Motta et al. (2009). We then fit an S- or Z-shaped curves to the ONIR data during the RPh, HtS and StH phases and determine the transition dates. Further, we fit the broken power-law to the DPh and Q data and obtain the start dates of quiescence. The details of the described procedure are explained in Appendix A and the start dates of each outburst phase (if this phase has been observed) are presented in Table 2. We also apply this fitting procedure to the failed outbursts, for which we identify ONIR phases with colors, similar to the phases of the regular outbursts.

Our definition of phases can be different from those in other works. For instance, the ONIR StH transitions defined in Kalemci et al. (2013) occur 2–6 days later than ours (compare our Table 2 to their table 2). At the same time, their transition dates defined by the X-ray spectral and timing properties are up to 20 days earlier. However, our start dates of the RHS and HtS of the 2007 outburst agree well with the transition dates obtained in Motta et al. (2009) using the X-ray spectral data.

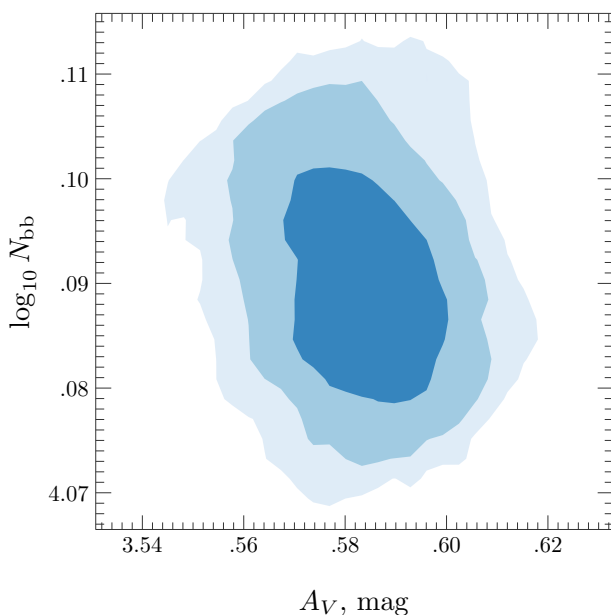
<sup>3</sup> [http://xte.mit.edu/ASM\\_lc.html](http://xte.mit.edu/ASM_lc.html)

<sup>4</sup> <https://swift.gsfc.nasa.gov/results/transients/weak/GX339-4/>

**Table 3.** ONIR filter effective wavelengths  $\lambda$ , zero-point fluxes  $F_0$  (Buxton et al. 2012) and derived extinction.

Filter	$\lambda$ (Å)	$F_0$ (Jy)	$A_\lambda$ (mag)
<i>V</i>	5450	3636	3.58
<i>I</i>	7980	2416	2.16 (+0.15)
<i>J</i>	12500	1670	1.00
<i>H</i>	16500	980	0.64

**Notes.** Extinction coefficients are calculated using interstellar extinction laws from Cardelli et al. (1989) and O’Donnell (1994).


**Fig. 3.** Joint posterior distribution of the model parameters. Contours correspond to 0.68, 0.95 and 0.99 probabilities.

### 3.2. Determination of extinction

We use the SS data from four regular outbursts to determine the extinction  $A_V$  towards the source. We select 236 nights, during which GX 339–4 was observed in all four ONIR filters. We convert magnitudes to fluxes using the zero-points given in Buxton et al. (2012, see also Table 2). Assuming that the SS spectra can be described by the blackbody model, we fit the data with the diluted Planck function modified by interstellar extinction:

$$F_{k,j} = 10^{-A_k/2.5} N_{\text{bb}} B_k(T_j), \quad (1)$$

where  $k$  corresponds to one of the ONIR filter (*V*, *I*, *J*, *H*), index  $j$  corresponds to the date,  $F_{k,j}$  is the model flux (in mJy),  $B_k$  is the value of the Planck function at the effective frequency of filter  $k$ ,  $T_j$  is the estimated blackbody temperature,  $A_k$  is the extinction (in magnitudes) in  $k$ -filter obtained using the model of Cardelli et al. (1989) with correction by O’Donnell (1994). The dimensionless normalization  $N_{\text{bb}}$  is assumed to be the same for all outbursts. It can be expressed through the effective radius of the irradiated disk  $R_{\text{irr}}$ , the distance to the source  $D$  and the disk inclination  $i$  as:

$$N_{\text{bb}} = 5.09 \times 10^4 \pi \left( \frac{R_{\text{irr}}/R_\odot}{D(\text{kpc})} \right)^2 \cos i. \quad (2)$$

We noticed that the fluxes in the *I* filter are systematically offset from the blackbody fits for any  $A_V$ . A possible reason

**Table 4.** Parameters of the system.

Mass ratio	$q$	$0.18 \pm 0.05^a$	
Orbital period	$P$	$1.76 \pm 0.01^a$ d	
Black hole mass	$M_1$	$5.9 \pm 3.6^a$	$M_\odot$
Inclination	$i$	$58 \pm 21^a$	deg
Distance	$D$	$8 \pm 2^b$	kpc
Binary separation	$a$	$11.6 \pm 5.1$	$R_\odot$
Roche lobe size	$R_{L,1}$	$6.1 \pm 3.2$	$R_\odot$
Maximum disk size	$R_{\text{tidal}}$	$5.9 \pm 2.6$	$R_\odot$
Effective radius of irradiated disk	$R_{\text{irr}}$	$3.0 \pm 1.1$	$R_\odot$

**Notes.** <sup>(a)</sup> From Heida et al. (2017). <sup>(b)</sup> From Zdziarski et al. (2004).

can be deviation of the irradiated disk spectrum from a simple blackbody. Therefore, for the fitting purposes, we introduce a correction  $\Delta A_I$  to the extinction in the *I* filter as an additional parameter. The best-fit parameters estimated using Bayesian inference are  $A_V = 3.58 \pm 0.02$  mag,  $\Delta A_I = 0.15 \pm 0.02$  mag and  $\log_{10} N_{\text{bb}} = 4.09 \pm 0.01$ . Fig. 3 shows the joint posterior distribution of the fitted  $A_V$  and  $N_{\text{bb}}$ .

Extinction can also be estimated using the color excess  $E_{B-V}$ . The value  $E_{B-V} = 0.94 \pm 0.19$  mag was derived from the X-ray absorption by Homan et al. (2005), while Zdziarski et al. (1998) give  $E_{B-V} = 1.2 \pm 0.1$  mag as a weighted mean obtained from different methods. Using interstellar absorption lines Buxton & Vennes (2003) got  $E_{B-V} = 1.1 \pm 0.2$  mag. These extinction estimates correspond to  $A_V$  between 2.9 and 3.7 mag (assuming  $R_V = 3.1$ , Cardelli et al. 1989). Thus, our estimate of  $A_V$  is well within the range of previously used values.

Our assumption that the blackbody normalization remains the same for all outbursts can be violated. For example, the effective disk radius in the LMXB XTE J1859+226 decreased with decreasing disk temperature (Hynes et al. 2002). It is unclear whether this happens due to the changes in the geometrical size of the disk or disk warping, or because of the propagation of the cooling wave (King & Ritter 1998). GX 339–4 shows complex behavior in its soft states (see Section 3.4 for the discussion), so it is possible that the normalization is indeed variable, which can systematically offset the inferred value of  $A_V$ . To address this issue we tried to fit  $T_j$  and  $N_{\text{bb},j}$  individually for each night, with  $A_V$  and  $\Delta A_I$  remaining global parameters. This problem is numerically unstable, because in the Rayleigh-Jeans regime (i.e. at high temperatures) Eq. (1) transforms into

$$F_{k,j} = 10^{-A_k/2.5} \frac{2\nu_k^2 k_B}{c^2} N_{\text{bb},j} T_j. \quad (3)$$

As a result, contributions of  $N_{\text{bb},j}$  and  $T_j$  cannot be easily decoupled and observations at higher energies (e.g. in UV) are required to properly fit temperatures and normalizations.

We also investigated the influence of the variable effective radius  $R_{\text{irr}}$  on the fitted value of  $A_V$  by introducing different normalizations for each outburst. We find no evidence that the variation in the normalization significantly affects the inferred value of  $A_V$ .

Using the obtained value of the blackbody normalization  $N_{\text{bb}}$  we now can estimate the characteristic size of the accretion disk. From the distance and the inclination of the binary system given in Table 4, we obtain  $R_{\text{irr}} = (3.0 \pm 1.1) R_\odot$ . We then estimate the binary separation  $a/R_\odot = 4.17(M_1/M_\odot)^{1/3}(1+q)^{1/3}P_{\text{day}}^{2/3}$  (see e.g. Frank et al. 2002), size of the primary Roche lobe  $R_{L,1}/a = 0.49/[0.6 + q^{2/3} \log(1 + q^{-1/3})]$  (Eggleton 1983) and the maximum disk size due to the tidal instability  $R_{\text{tidal}}/a = 0.60/(1 + q)$

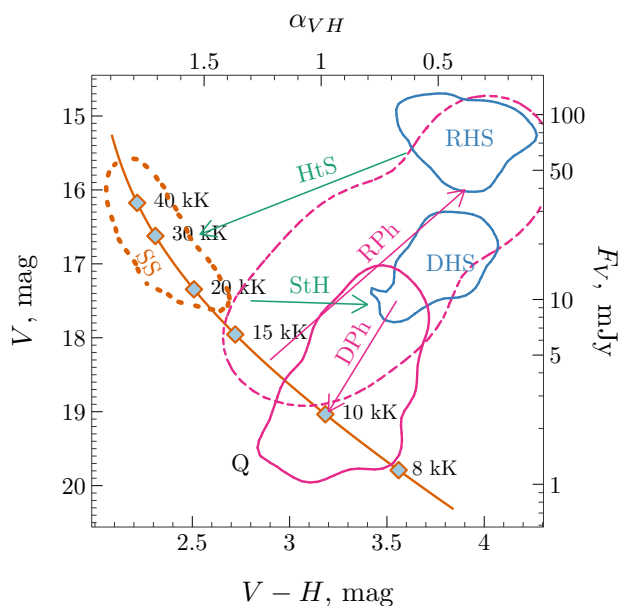


**Fig. 4.** Evolution of magnitudes and colors of GX 339–4 throughout the outburst.  $V$  and  $V-H$  are observed magnitudes and colors,  $F_V$  is corrected for the interstellar extinction flux and  $\alpha_{VH}$  is the intrinsic spectral slope, computed assuming  $A_V = 3.58$  mag (see Eq. 5). Dashed pink contour corresponds to the RPh, top-right solid blue contour – to the RHS, top solid green arrow – to the HtS transition, dotted orange contour – to the SS, bottom solid green arrow – to the reverse StH transition, bottom solid blue contour – to the DHS, solid pink contour – to the DPh. Solid orange line gives the model blackbody curve with  $\log_{10} N_{\text{bb}} = 4.09$ , see Eq. (1) and filled blue diamonds along the curve correspond to the temperatures marked on the right. The quiescent state is marked with letter Q in the lower part of the diagram.

(Paczynski 1977; Warner 1995). This allows us to compare the parameters of GX 339–4 to its “twin” system XTE J1550–564 (Muñoz-Darias et al. 2008).

Analysis of the ONIR light curves of the 2000 outburst of XTE J1550–564 (Poutanen et al. 2014) showed that the effective radius of the irradiated disk of XTE J1550–564,  $R_{\text{irr}} \approx 4.1 R_{\odot}$ , is 40% smaller than the maximum disk size of  $6.9 R_{\odot}$ . Although GX 339–4 and XTE J1550–564 binary systems have similar sizes (Orosz et al. 2011; Hynes et al. 2003b; Heida et al. 2017), the major difference is the binary mass ratio  $q$ , which is of the order of 0.033 for XTE J1550–564 and 0.18 for GX 339–4 (see Table 4). Larger mass ratio leads to a smaller primary Roche lobe size, limiting the maximum size of the accretion disk.

### 3.3. Outburst template

In this section we study the  $V-(V-H)$  CMD of the regular outbursts to construct the outburst template. We use data from a given phase (RPh, RHS, SS, DHS and DPh) to compute the 90 per cent density contour (with the exception of the 2004–2005 outburst, whose RHS we omit because it is systematically fainter than that of the other regular outbursts). The obtained template is shown in Fig. 4 and we further use it to study the similarities between regular outbursts and the peculiarities of the failed ones.

We compute the intrinsic spectral slopes  $\alpha_{ij}$  (where the flux depends on frequency as  $F_{\nu} \propto \nu^{\alpha}$ ), from the observed colors as

$$\alpha_{ij} = \frac{m_i - m_j - (A_i - A_j) - 2.5 \log(F_i^0 / F_j^0)}{2.5 \log(\lambda_i / \lambda_j)}, \quad (4)$$

where  $i, j$  correspond to ONIR filters ( $V, I, J$  or  $H$ ),  $m_i - m_j$  is the observed color,  $A_i$  and  $A_j$  are the interstellar extinctions,  $\lambda_i$  and  $\lambda_j$  are the effective wavelengths, and  $F_i^0$  and  $F_j^0$  are the zero-point fluxes in  $i$  and  $j$  filters, respectively (see Table 3). Equation (4) for  $V$  and  $H$  filters can be reduced to

$$\alpha_{VH} = -0.84 (V - H) + 0.69 A_V + 1.16. \quad (5)$$

The observed RPh begins with the spectrum resembling blackbody with temperature of  $T \approx 14$  kK. The spectrum then reddens as it enters the RHS, reaching  $V-H \approx 4$  mag. During the HtS transition which takes 5–10 d, the spectrum becomes bluer. This evolution may be attributed to the quenching of the red non-thermal component. In the SS the source moves along the blackbody track (see Fig. 4, solid orange curve) towards upper-left part of the CMD, indicating a temperature increase from roughly 30 up to 50 kK. In 100–200 d, ONIR fluxes decrease and the temperature drops substantially. This marks the end of the SS and the beginning of the StH transition, which occurs at  $T \approx 20$  kK. The StH transition takes 11–18 d and the source moves almost horizontally on the  $V-(V-H)$  CMD, indicating an increase of flux in  $H$  filter at almost no changes in  $V$ . GX 339–4 spends 20–30 d in the DHS (although, in 2007 it lasted for more than 100 d) and after that it enters the DPh. During the next  $\sim 50$  d, the observed ONIR fluxes drop dramatically and the spectra become bluer. The Q phase does not follow the blackbody track and shows a substantial (up to 1.5 mag) variability of  $V-H$  color, unlike in other systems (see Kalemci et al. 2013; Poutanen et al. 2014).

We find that the colors and magnitudes of RHS are systematically different from those of DHS. The RPh is somewhat bluer than the DPh for the same  $V$  magnitude (Fig. 4). The SS contour (solid orange line) is elongated along the blackbody track, but there is some spread of the data points around the model. This is likely caused by the variability due to superhumps (Kosenkov & Veledina 2018).

The spread of colors in the Q phase is peculiar. It cannot be explained by the measurement errors (see Fig. 5a, bottom left corner), as it exceeds the typical error by a factor of 10. Interestingly, most of the Q phase data points lie below the blackbody line, i.e. the colors are typically bluer than the blackbody that has the same  $V$ -flux. We also note that the lowest observed blackbody temperature when the source enters the Q-phase is still above the hydrogen ionization limit.

### 3.4. Regular outbursts

In this section we describe the properties of each outburst. We stress the peculiarities and deviations from the common pattern discussed above. The 2002–2003 outburst is the only one with many observations of the initial RPh (filled pink upward-facing triangles in Fig. 5). This outburst was also observed during the HtS transition (filled green downward-facing triangles). Thus, we can trace the evolution of GX 339–4 before and after the RHS (filled blue circles) and compare it to the decay stages: StH transition (open green triangles), DHS (open blue circles) and DPh (open pink triangles). Interestingly, after the HtS transition, the flux in  $H$  filter showed no visible daily-timescale variability (see Fig. 5b; also Homan et al. 2005). In about 40 d (MJD 52440), when the flux started to decrease, the variability, which was previously attributed to superhumps (Kosenkov & Veledina 2018), became apparent. At the time of this change, the ASM fluxes and ASMB/A hardness ratio had a local minimum (see Fig. 5b,c).

The 2004–2005 outburst was fainter, both in the X-rays and in ONIR, as compared to other regular outbursts (see Figs. 1 and

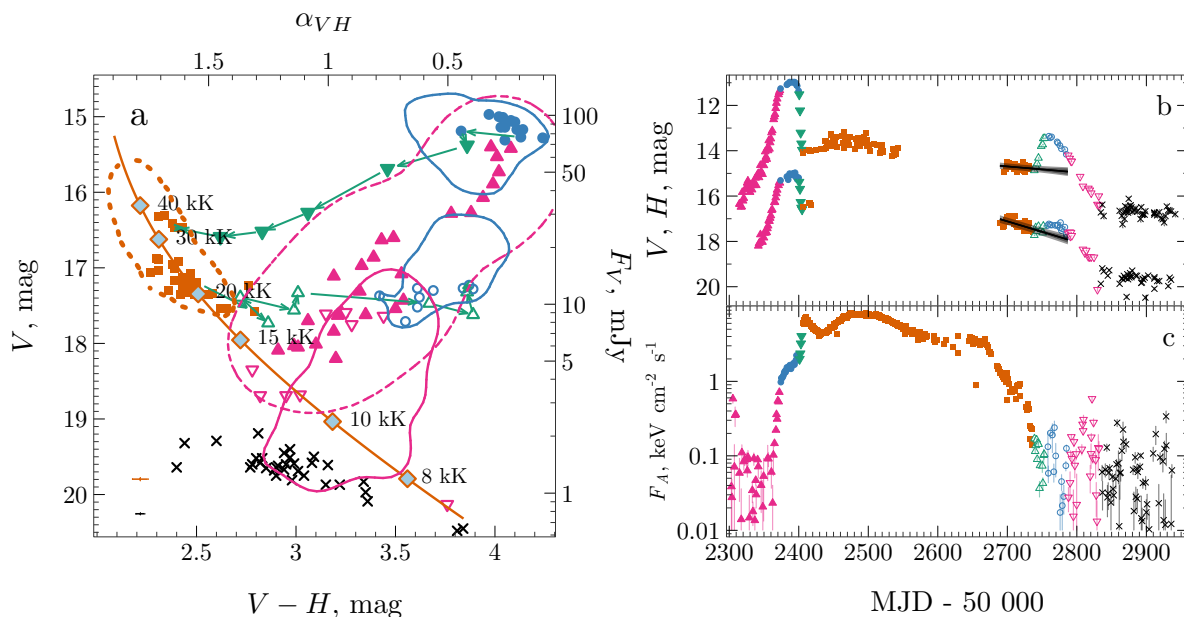


**Fig. 5.** (a)  $V$  versus  $V - H$  color-magnitude diagram of the 2002–2003 outburst. Filled upward-facing pink triangles correspond to the RPh, filled blue circles – to the RHS, filled downward-facing green triangles – to the StH transition, filled orange squares – to the SS, open upward-facing green triangles – to the DHS, open blue circles – to the DHS, open downward-facing pink triangles – to the DPH, black crosses – to the Q. Contours are the same as in Fig. 4. The typical  $1\sigma$  errors are shown in the lower left corner: the top orange cross corresponds to the bright states and is comparable to the plot symbol size, the bottom black cross corresponds to the quiescent state data, where observational errors are substantial. (b) ONIR  $H$  (top) and  $V$  (bottom) light curves of the same outburst. Symbols are the same as in panel (a). Errors are  $1\sigma$  and error bars are comparable to the symbols size. Solid black line represents the model, fitted to the part of the SS data. The grey area around the line denotes  $1\sigma$  errors and also includes the contribution from the intrinsic scatter. (c) ASMA X-ray light curve.

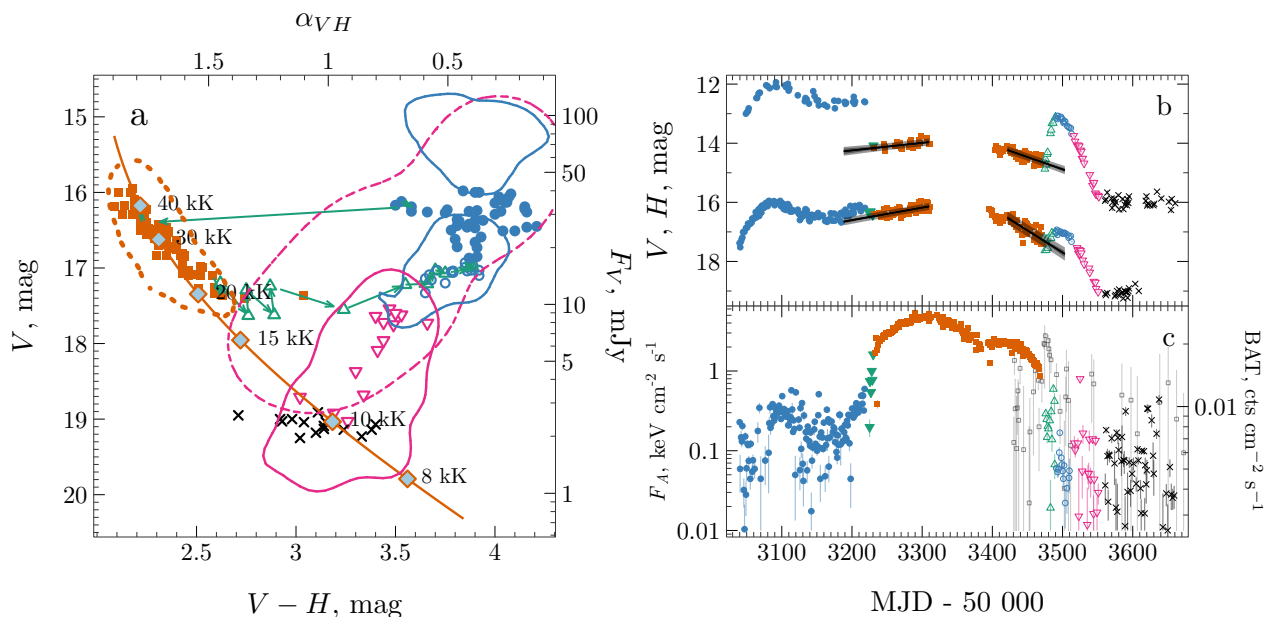


**Fig. 6.** Same as Fig. 5, but for the 2004–2005 outburst. (c) The BAT data are shown with open gray squares starting from the second half of the 2004–2005 outburst. Errors are  $1\sigma$ .

2). The same conclusion can be reached from Fig. 6a, where the RHS (filled blue circles) are located between two template (RHS and DHS) contours (blue solid lines). The duration of the RHS,  $\approx 180$  d, is longer than that in the other outbursts (20–75 d). The  $V$ -filter flux increased after the transition to SS, and then decreased together with the decreasing ASM fluxes (Fig. 6b,c). The DHS points are located well within the template contour, and the

corresponding fluxes are only marginally lower than those of the RHS, in contrast to other regular outbursts.

The 2007 outburst demonstrates unusually short SS and a long DHS. Both ASM and ONIR fluxes decayed after the HtS transition (Fig. 7b,c), and the decay took about 100 d, as compared to typical 250–300 d for other outbursts. On the contrary, the DHS lasted over 100 d, in contrast to typical  $\sim 50$  d for other

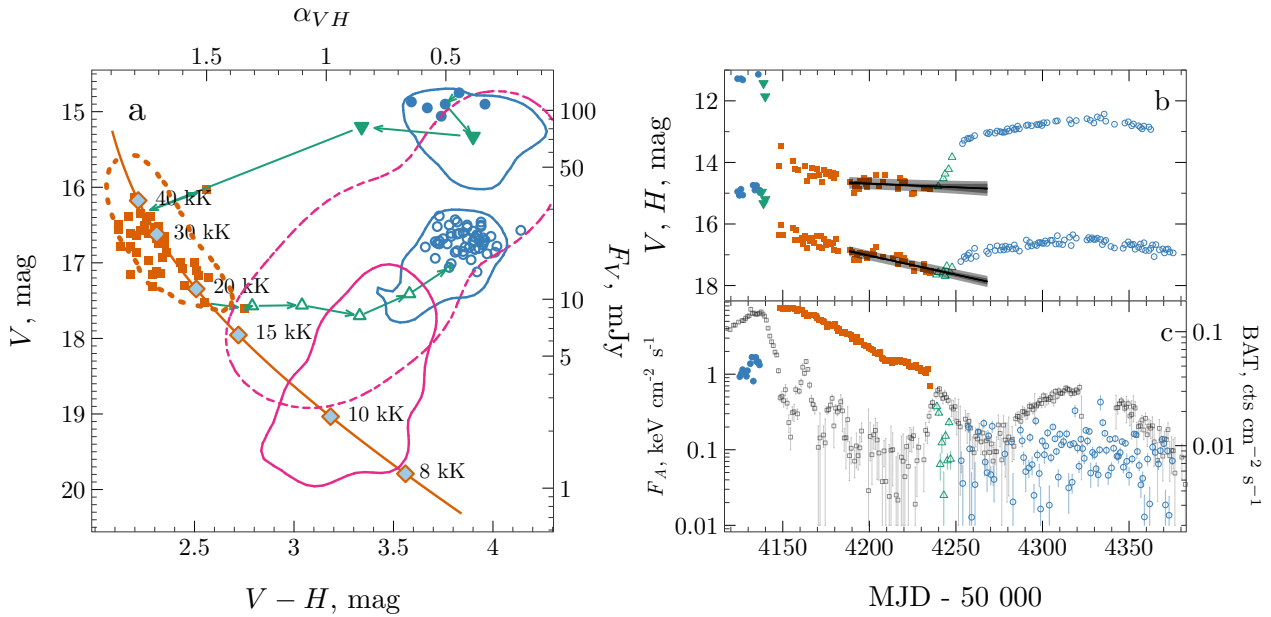


Fig. 7. Same as Fig. 6, but for the 2007 outburst.

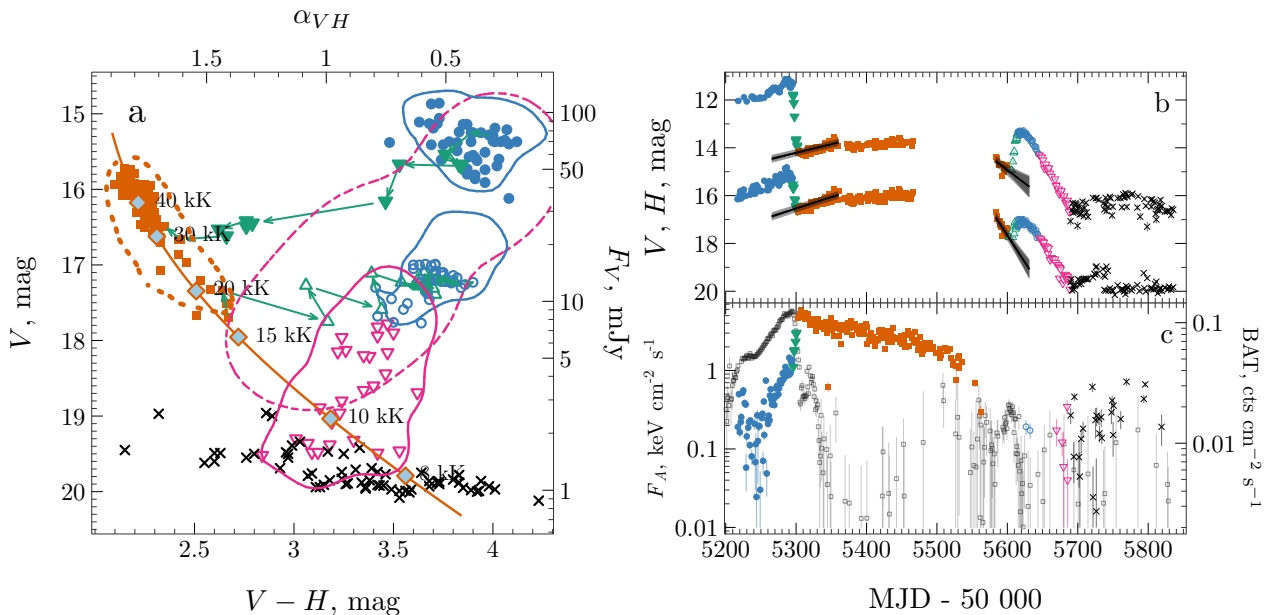


Fig. 8. Same as Fig. 6, but for the 2010–2011 outburst.

outbursts. It is even possible that this phase continues throughout the first half of 2008.

The ONIR light-curves of the 2010–2011 outburst show peculiar trend discontinuity during the SS (around MJD 55360, see Fig. 8b). Nevertheless, all SS data points align well with the blackbody model on the CMD (Fig. 8a), hence, the observed break is caused by the sudden decrease of the color disk temperature.

### 3.5. Failed outbursts

We have three failed outbursts in 2002–2011, in 2006 (see Figs. 9), in 2008 (see Fig. 10) and in 2009 (see Fig. 11), when GX 339–4 does not enter the SS, in contrast to regular outbursts. The ONIR peak fluxes are a few times smaller than the RHS of

regular outbursts, however, the colors are the same. The duration of different phases of failed outbursts is comparable to those of regular outbursts.

The 2006 and 2009 failed outbursts have similar duration and peak magnitudes. The light curves of the 2009 failed outburst have double-peaked profile (both in the ONIR and the X-rays) and the  $V - H$  colors of both peaks are the same. Interestingly though, the brightest episode of the 2009 outburst resembles the RHS of the 2004–2005 regular one in terms of phase duration, typical ONIR magnitudes and colors (compare Fig. 6b and Fig. 11b, blue dots). This similarity makes it harder to distinguish between regular and failed outbursts at early phases.

The 2008 failed outburst peak is about 0.5 magnitude fainter than that of the other failed outbursts. It consists of two peaks (Russell et al. 2008; Kong 2008), both of them having colors and

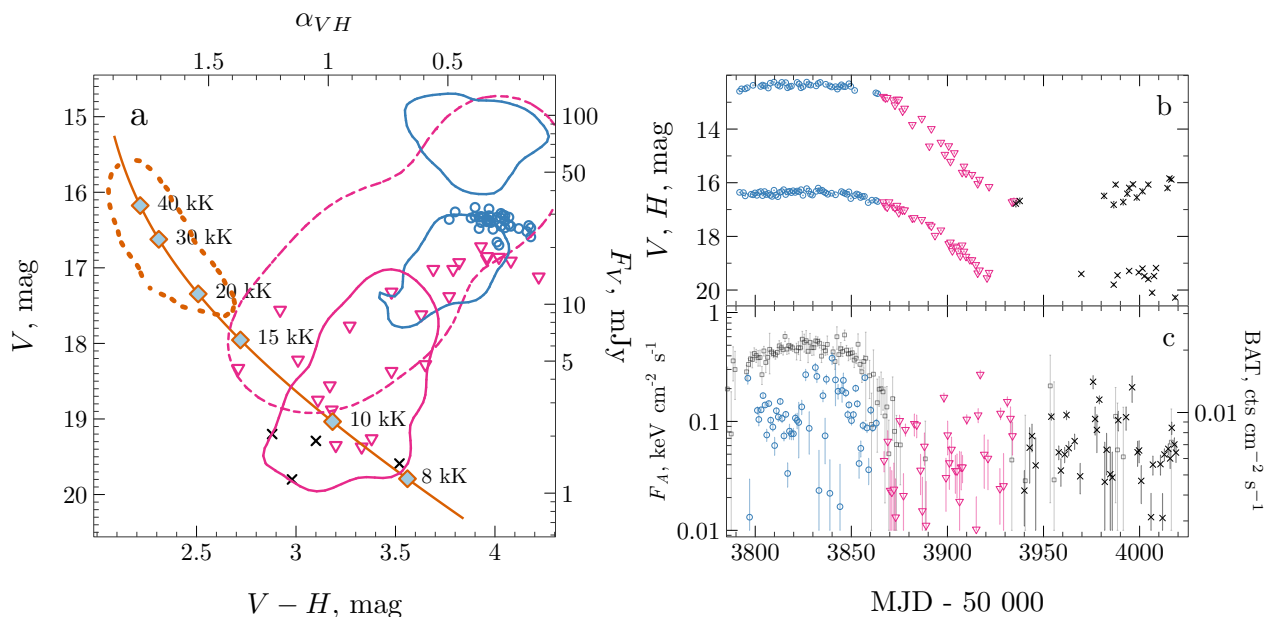


**Fig. 9.** Same as Fig. 6, but for the 2006 failed outburst. We use blue circles to mark the bright phase of the outburst and black crosses to mark the quiescent state. The transition is marked with pink triangles.

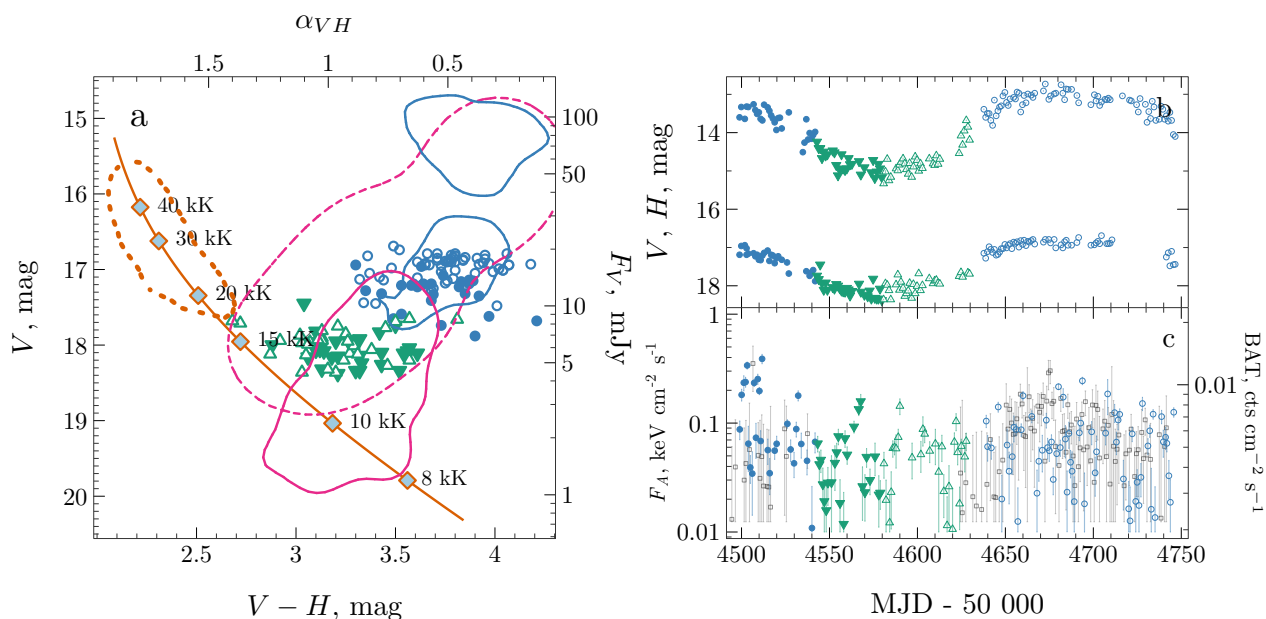


**Fig. 10.** Same as Fig. 9, but for the 2008 failed outburst. We use filled green triangles to mark the transition from the initial bright phase to the faint phase and open green triangles to mark the rebrightening.

magnitudes typical to the DHS (see Fig. 10a). The second brightening is, on the other hand, considerably longer than the typical DHS. Between the two peaks the source dims and becomes bluer as if it were going to the SS, similar to the HtS transition. However, it reddens again and returns back to the DHS along a similar track on the CMD. Therefore, we color these phases on the CMD as HtS and StH. We note that the timescales are somewhat larger (40–50 d as opposed to 10–20 d; see Fig. 10b, Table 2). Though we consider the 2008 outburst as a separate one, there is a possibility that it can be a continuation of the exceptionally long 2007 outburst.

We note that the distinction between the failed and regular outbursts is not possible from the ONIR data alone at their

earlier stages. However, it might be possible using the peak  $V$ -magnitude. If the source is brighter than  $V = 16$  mag during the RHS, it will transit to the SS. On the other hand, if it is fainter, the outburst can be either regular (2004–2005 outburst, see Fig. 6) or failed (2009 outburst, see Fig. 11).

### 3.6. Evolution of the non-thermal component

It is known that the changes of ONIR colors during the HtS and StH transitions are related to quenching/recovery of the red, non-thermal component (see e.g. Fender et al. 1999; Jain et al. 2001; Corbel & Fender 2002). To understand the origin of the non-thermal emission, it is important to obtain a reliable estimate



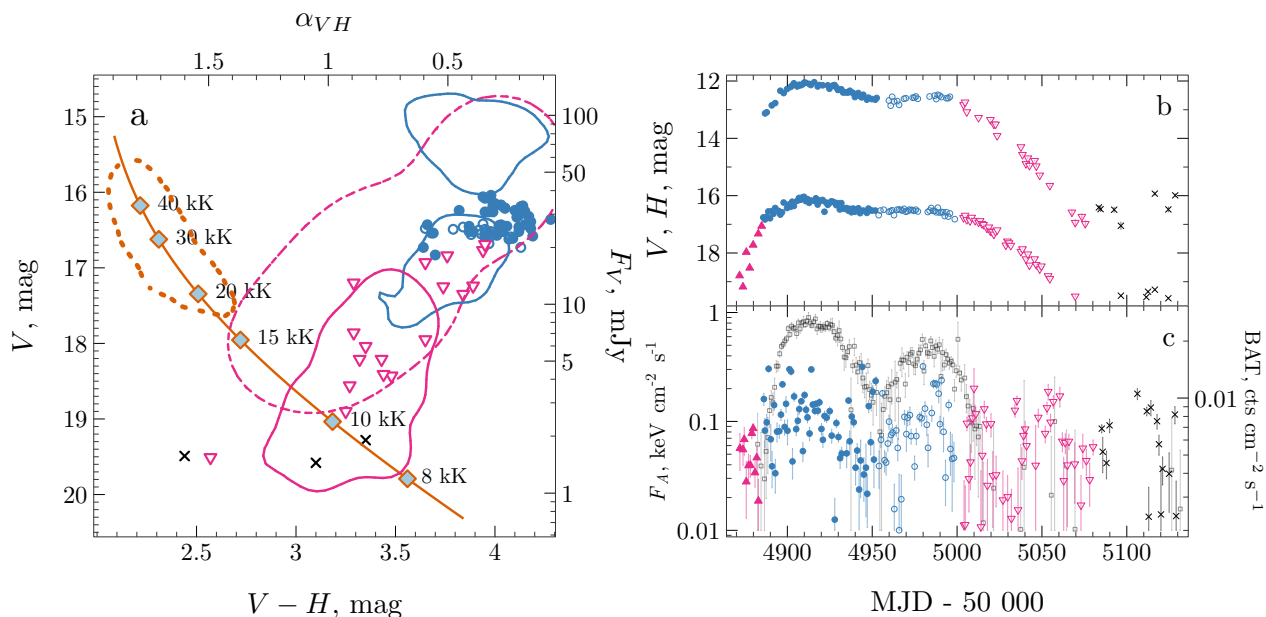


**Fig. 11.** Same as Fig. 9, but for the 2009 failed outburst.

of its spectral shape by subtracting the contribution of the thermal (disk) component. The task is, however, complicated by the fact that the spectrum of the thermal component (e.g. disk temperature) is an unknown function of time. The spectral index of the non-thermal component may allow us to distinguish between two alternatives: the jet (Fender 2001; Gallo et al. 2007; Uttley & Casella 2014) and the hot flow (Veledina et al. 2013; Poutanen & Veledina 2014; Kajava et al. 2016). The contribution of the disk can be estimated by fitting the SS light-curves in different filters, and extrapolating the obtained fit to the transitions and the hard state (see, e.g., Buxton et al. 2012; Dinçer et al. 2012; Poutanen et al. 2014). The weakness of this approach is related to freedom in the choice of the fitting function and the fitting interval, which leads to an uncertainty in the spectrum of the non-thermal component.

In general, the emission of the irradiated accretion disk is expected to follow the fast rise – exponential decay profile (and a constant level of emission in quiescence, see e.g. Chen et al. 1997). The exponential decay profile was fit to the 2000 outburst data of XTE J1550–564 (Poutanen et al. 2014), while GX 339–4 shows both episodes of decay and rise during the SS. Therefore, we fit parts of the SS light curves using the following model:

$$m_j(t) = m_j^0 + \mu_j(t - t^0) + \epsilon_j, \quad (6)$$

where  $\mu_j$  is the slope, which can be positive or negative. Here  $m_j$  is the observed magnitude in  $j$ -th ONIR filter,  $m_j^0$  is the constant,  $t$  is the time and  $t^0$  is either the beginning (if the fitted data set covers the first part of the SS) or the end time of the fitted data set (if it covers the last part of the SS), and  $\epsilon_j$  is the intrinsic scatter, which is partially caused by superhump variability (Dinçer et al. 2012; Kosenkov & Veledina 2018). We use Bayesian inference to estimate these parameters and list them in Table 5.

Once the fit to the SS is obtained, we extrapolate the model for 30 days from the start or the end of the SS, which usually cover the transition phase and a part of the hard state. The errors on the fluxes of the non-thermal component are mostly coming from the uncertainties in the parameters of the fitted model and

they increase towards the hard state. On the other hand, the contribution of the disk also drops, and it falls down to about 5% in the RHS.

The fitted models are shown in Figs. 5-8(b) with the solid black lines. The gray areas around the model denote  $1\sigma$  uncertainties. The model curve spans over the SS data used for fitting (orange squares), the transition phase (if present, green triangles) up to the nearest hard state (blue circles). The total spectra and the spectra of the non-thermal component are shown in Fig. 12. The fluxes are corrected for the interstellar extinction assuming  $A_V = 3.58$  mag (see Sect. 3.2).

In the majority of cases, both the hard state and the state transition spectra of the non-thermal component appear to be nearly flat ( $\alpha_{VH}^{\text{nth}} = 0.06 \pm 0.12$ , the best examples are the 2004–2005 DHS and 2010–2011 RHS, see Fig. 12c\*,e\*). During the transitions, the spectral shape of the non-thermal component is stable. We also note that there is no apparent difference between spectral shapes of that component in the StH and HtS transitions.

The spectral slope  $\alpha_{\text{ONIR}}$  is affected by the assumed value of  $A_V$ . The impact of  $A_V$  can be estimated using Eq. (5). For a relatively low value of  $A_V \approx 3.0$  mag (Kong et al. 2000; Homan et al. 2005),  $\alpha_{VH}^{\text{nth}} = -0.34$ , while for a relatively high  $A_V = 3.7$  mag (Zdziarski et al. 1998; Buxton et al. 2012) we get  $\alpha_{VH}^{\text{nth}} = 0.15$ . The changes in  $A_V$  are also reflected in the curvature of the blackbody track on the CMD located within the SS contour (see discussion in Section 4.1).

To illustrate the results of our spectral decomposition, we select a sample of the RHS, HtS, SS, StH and DHS data of each regular outburst. We fit a model consisting of a power law of index  $\alpha = 0$  to account for the non-thermal component (except for the SS) and a blackbody to the data corrected for interstellar extinction. The blackbody normalization is allowed to vary between the outbursts. The results are shown in Fig. 13. This simple model reproduces the data very well.

### 3.7. Broad-band spectra in the hard state

The hard-state mid-IR spectra of GX 339–4 can help us identify the nature of the non-thermal component. GX 339–4 was

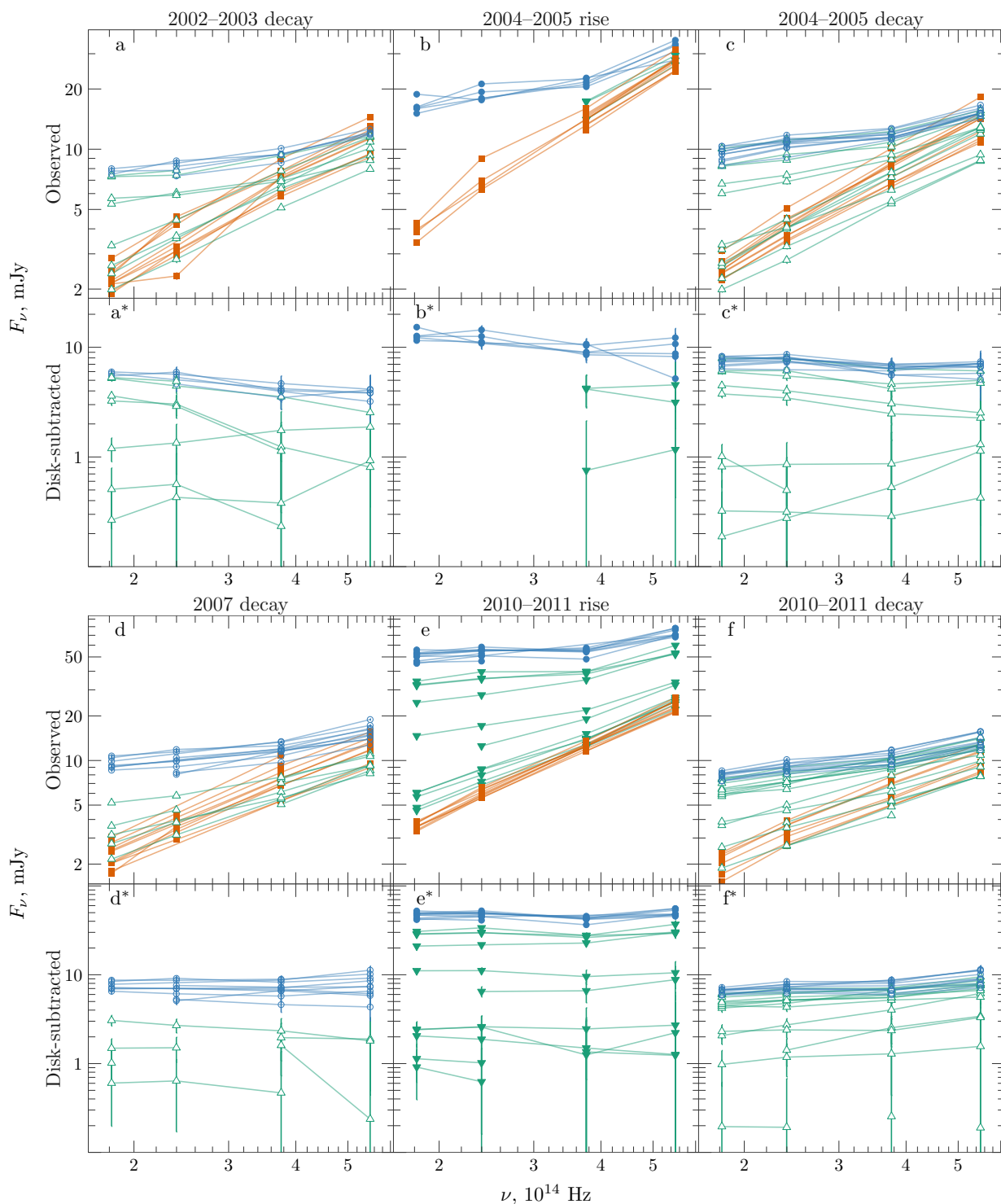


**Fig. 12.** Sample of spectra from the soft state (orange squares), transition (green triangles) and the hard-state spectra (blue circles). Open symbols are for the soft to hard state transitions, while the filled symbols are for the hard to soft state transitions. Upper panels (a-f) show total observed spectra of the decaying part of the 2002–2003 outburst, rising and decaying parts of the 2004–2005 outburst, the 2007 outburst and the rising and decaying parts of the 2010–2011 outburst, respectively. Lower panels (a\*–f\*) show corresponding spectra after subtraction of the thermal component. Fluxes are corrected for the interstellar extinction, errors are  $1\sigma$ .

observed in the mid-IR with *WISE* on MJD 55265.88–55266.88 (Gandhi et al. 2011). The 13 mid-IR spectra can be divided into two groups. At lower fluxes, the *WISE* spectra are nearly flat (see spectra #1, 2, 7, and 8 in their fig. 3) and lie on the continuation of the ONIR non-thermal component. At higher fluxes, the spectra are much softer and most of them have a large curvature (e.g. spectra #3–6, 9, 12–13; see also blue triangles in Fig. 14).

The source shows strong, by a factor of three, variability in all four *WISE* filters on the timescales of hours (see fig. 2a and table 1 in Gandhi et al. 2011). Variability amplitude increases towards longer wavelengths. Extrapolation of the *WISE* spectra to the ONIR bands predict an order of magnitude variation there. However, the observed ONIR non-thermal component is nearly constant. This suggests that there are two non-thermal compo-

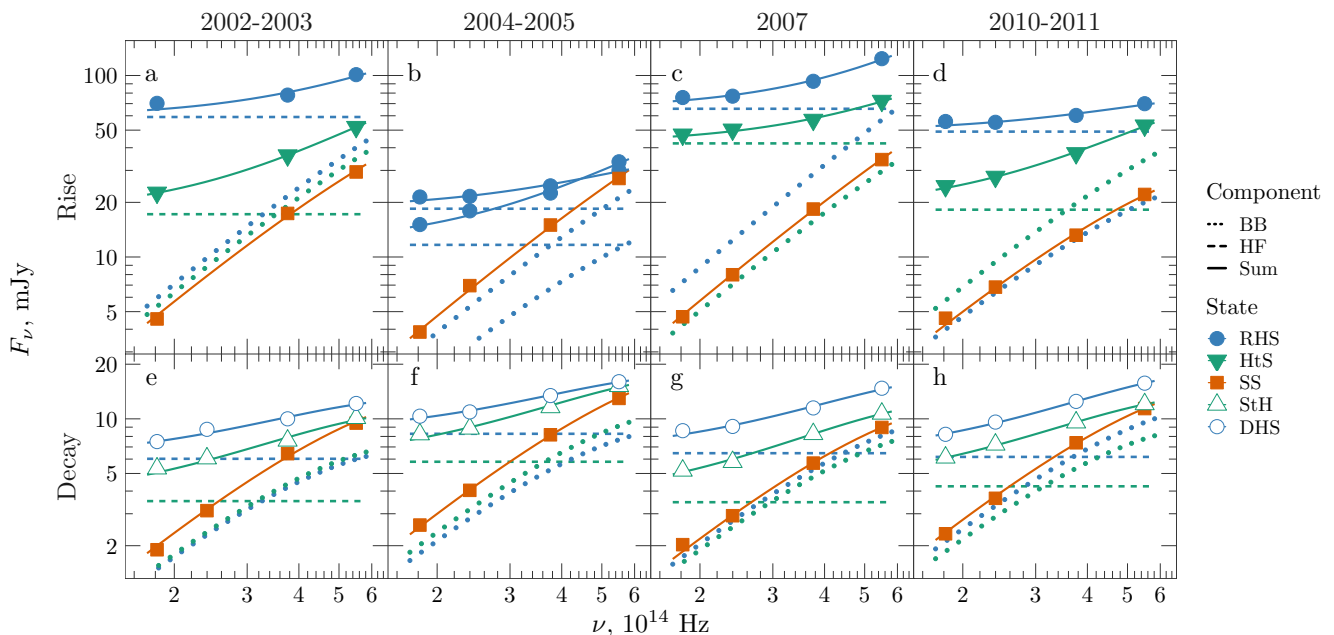


**Fig. 13.** Selected spectra of the rising (upper panels) and decaying (lower panels) stages of regular outbursts.  $1\sigma$  errors are comparable to the symbol size. Solid orange and dotted blue and green lines correspond to the blackbody (BB) component in the soft and hard states and transitions, respectively. Dashed blue and green lines correspond to the power-law spectra of the hot flow (HF). Solid lines give the sums of the corresponding blackbody and the hot flow components. In panel (b) we do not plot HtS spectrum because there are no observations with simultaneous measurements in three or more ONIR filters. Instead, we show two RHS spectra, separated by  $\sim 150$  d, to highlight the evolution of both non-thermal and disk components (see also Fig. 6).

nents: one highly variable dominating during high mid-IR flux episodes and another, more stable, emitting in a broad range from mid-IR to ONIR. There is a caveat though that the typical *WISE* exposure is about 10 s, which is much smaller than the typical 300 s exposure in the ONIR bands.

To understand the nature of these components, we try to construct the source broad-band spectra. All available 13 *WISE* observations occurred during 24 hours on MJD 55265.9–55266.9. There is one observation on MJD 55266.3481, which is just 16 min before the SMARTS observations on MJD 55266.3594. In addition we also choose two nearest *WISE* observations 1.7 h before and after the quasi-simultaneous one, on MJD 55266.28 and on 55266.41. In order to estimate contribution from the disk blackbody, we use the SS ONIR observation on MJD 55301.36, because after the HtS transition the ONIR flux was nearly constant (see Fig. 8). Furthermore, we select the closest in time ATCA 5.5 and 9 GHz measurements obtained on MJD 55269.80 (Corbel et al. 2013b). Albeit the radio and mid-IR data are taken on different dates, the extrapolation of the hard radio spectrum matches the high-flux *WISE* data. The connection between the radio and mid-IR fluxes and their high variability on short timescales are hallmarks of the jet emission as seen in blazars (Tavecchio 2017; Zacharias 2018). A simple jet model of Blandford & Königl (1979), which was often invoked to explain the radio to NIR spectra of GX 339–4 (see e.g. Corbel & Fender 2002; Gandhi et al. 2011; Rahoui et al. 2012; Corbel et al. 2013a), does not address the presence of the sharp cutoff in the mid-IR spectra and the dichotomy of mid-IR spectral slopes.

We suggest that the broad-band spectrum of GX 339–4 consists of (at least) three components. We model the disk component by the blackbody. We use a power law with spectral index close to zero, which transforms to Rayleigh-Jeans spectrum at lower-frequencies, to model the hot flow. The jet is described by a power law with a high-frequency cutoff. The model can be

described by the following equations:

$$\begin{aligned}
 F_{\nu}^{\text{bb}} &= N_{\text{bb}} B_{\nu}(T), \\
 F_{\nu}^{\text{hf}} &= N_{\text{hf}} \left( \frac{\nu}{10^{14} \text{ Hz}} \right)^{\alpha} \left\{ 1 - \exp \left[ - \left( \frac{\nu}{\nu_{\text{hf}}} \right)^{2-\alpha} \right] \right\}, \\
 F_{\nu}^{\text{jet}} &= N_{\text{jet}} \left( \frac{\nu}{10^{10} \text{ Hz}} \right)^{\beta} \exp \left[ - \left( \frac{\nu}{\nu_{\text{jet}}} \right)^{\gamma} \right], \\
 F_{\nu}^{\text{tot}} &= F_{\nu}^{\text{bb}} + F_{\nu}^{\text{hf}} + F_{\nu}^{\text{jet}},
 \end{aligned} \tag{7}$$

where  $F_{\nu}^{\text{bb}}$ ,  $F_{\nu}^{\text{hf}}$ ,  $F_{\nu}^{\text{jet}}$  and  $F_{\nu}^{\text{tot}}$  are the model fluxes of the disk, hot flow, jet components and their sum, respectively,  $N_{\text{bb}}$ ,  $N_{\text{hf}}$  and  $N_{\text{jet}}$  are the model normalizations,  $T$  is the blackbody temperature,  $\nu_{\text{hf}}$  is the low-frequency cutoff of the hot flow component,  $\nu_{\text{jet}}$  is the high-frequency cutoff of the jet spectrum,  $\alpha$  and  $\beta$  are the corresponding power-law slopes, and  $\gamma$  is the index of the super-exponential cutoff. The value of  $\log N_{\text{bb}}$  is fixed at 4.09 derived in Sect. 3.2.

Fig. 14 shows the RHS spectra of GX 339–4 as observed by ATCA, *WISE* and SMARTS together with one SS ONIR spectrum as well as the best-fit models. We assume that the hot flow spectrum is the same for all three mid-IR spectra. For the jet component, we use different cutoff frequencies, because normalization and power-law slope are determined by the shape of the radio data, which is the same in all cases. Due to the difference in the exposure times of *WISE* (<10 s) and SMARTS (300 s) as well as some systematic uncertainties in absolute flux of *WISE*, we apply additional cross-calibration factor to the mid-IR fluxes, which is treated as a free parameter. The best-fit parameters are given in Table 6.

We see that on MJD 55266.28 the jet outshines the hot flow by a factor of 2–3 in W4 and W3 filters. The overall, radio to ONIR, spectrum cannot be described by a broken power law plus a blackbody. This implies that the spectrum above

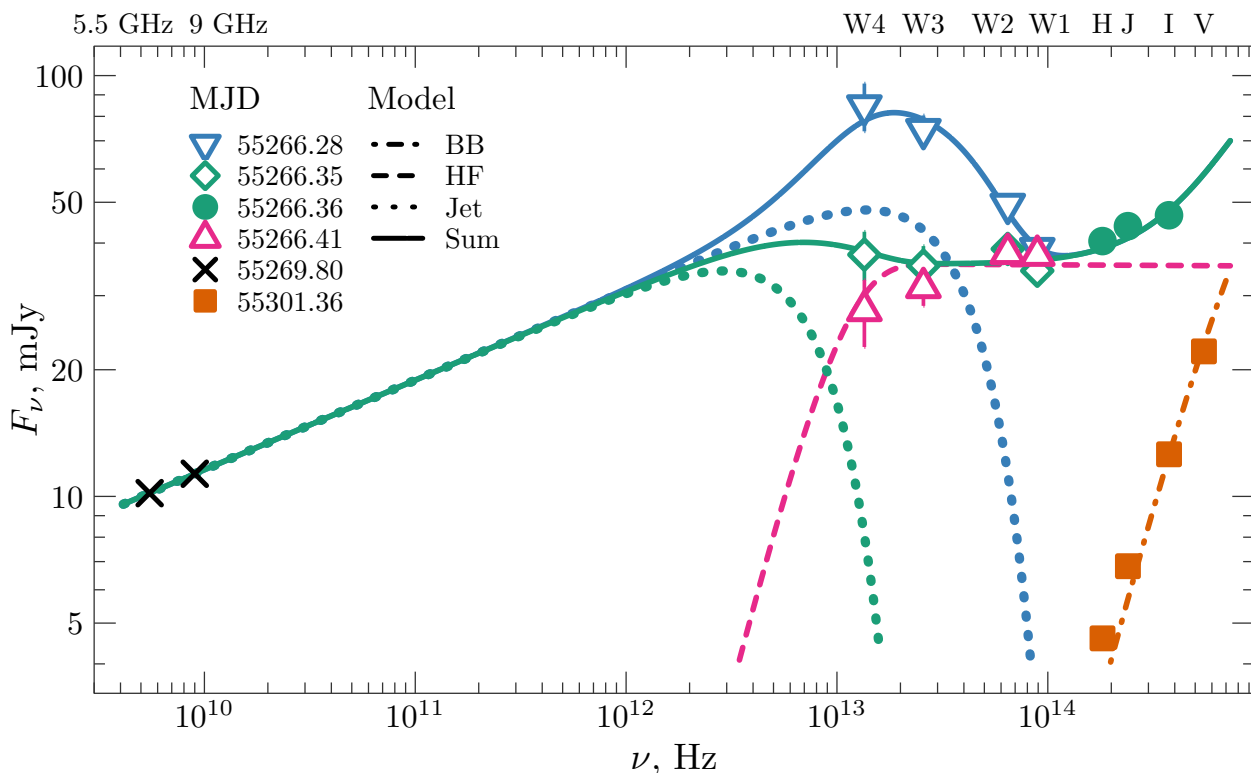


**Fig. 14.** Broad-band spectra of GX 339–4 using the radio ATCA, mid-IR *WISE* and ONIR SMARTS data. The figure shows four distinct spectral shapes for the source. Orange squares show the soft-state data from MJD 55301.36, the filled green circles and open green diamonds are the quasi-simultaneous ONIR and mid-IR data on MJD 55266.35. Open blue downward-facing triangles and open pink upward facing triangles show the mid-IR spectra measured 1.7 h before and after the quasi-simultaneous observation, respectively. Black crosses are one of the closest available ATCA radio observation (MJD 55269.80) that is used to constrain the jet properties. The lines show different model components: dot-dashed orange line is the blackbody component, dashed pink line is for the hot-flow component, the dotted lines correspond to the jet model with different cutoff frequencies, and solid lines give the sum of the three (blackbody + hot flow + jet) components. The sum of the blackbody and hot flow components for MJD 55266.41 is not shown for convenience, because it fully coincides with the hot flow curve in the mid-IR.  $1\sigma$  errors are comparable with the symbol size. The *WISE* fluxes are adjusted by the normalization factors inferred from the fit (see Table 6).

$\sim 3 \times 10^{13}$  Hz is not consistent with an optically-thin, power-law-like synchrotron spectrum predicted by a standard jet model of Blandford & Königl (1979). The sharp cutoff below  $10^{14}$  Hz cannot be described even by a simple exponential cutoff but is well fit only by a super-exponential with the index  $\gamma \approx 2$ . If we interpret the power-law spectrum from radio to the mid-IR as a combination of self-absorbed synchrotron peaks, such a cutoff can only be obtained if the electron distribution producing the mid-IR emission has a very steep slope.

On MJD 55266.35 the jet likely contributes to the W4 filter, but the hot flow takes over at higher frequencies. The *WISE* spectrum obtained on MJD 55266.41 is the hardest one with  $\alpha = 0.16$  having a clear curvature below  $2 \times 10^{13}$  Hz, which can be associated with the synchrotron self-absorption frequency of the hot-flow spectrum (dashed pink line). Therefore the hot flow likely dominates in all mid-IR filters and contributes to the ONIR flux together with blackbody component. The measurement of the low-frequency cutoff allows us to constrain the size of the hot flow (corona) to be (eq. 13 in Veledina et al. 2013)  $R_{\text{hf}} \approx 3 \times 10^9 (10^{13} \text{ Hz}/\nu_{\text{hf}}) \approx 2.7 \times 10^9$  cm, which corresponds to 900 Schwarzschild radii for a 10 solar-mass black hole. For this observation, we obtain only an upper limit on the jet cutoff frequency, because the contribution of the jet to the mid-IR is negligible.

## 4. Discussion

### 4.1. ONIR spectral properties

The magnitude-magnitude diagrams (see Buxton et al. 2012) can be used to emphasize the difference between hard and soft states and highlight the state transition tracks. However, these diagrams do not provide sufficient information about the shape of the spectra in each of the observed states and make it harder to separate RHS and DHS data points as they roughly follow the same broken power-law track (together with the data from quiescence, see e.g. fig. 9 in Buxton et al. 2012). Alternatively, one can use color-magnitude diagrams (Maitra & Bailyn 2008; Russell et al. 2011; Poutanen et al. 2014). CMD plots benefit from the fact that they highlight both changes in the observed fluxes and in the shape of the spectra. The characteristic hysteresis pattern tracked by the source on the CMD can be related to the hysteresis observed in the X-ray data (Poutanen et al. 2014). In three out of four regular outbursts, GX 339–4 was observed to have nearly identical HtS and StH transitions patterns on a CMD (see Sect. 4.2 for a discussion; also fig. 1 in Corbel et al. 2013b, fig. 1 in Muñoz-Darias et al. 2008), while during the HtS transition of the rising phase of the 2002–2003 outburst the X-ray fluxes were a few times smaller than the typical values (Fig. 2b,c). Interestingly, though the 2002–2003 HtS transition starts at lower ONIR fluxes, it arrives at the same SS flux with a color temperature of 30–35 kK.

**Table 5.** Best-fit parameters for model (6) to the light curves in the soft state. Errors are  $1\sigma$ .

Filter	$t^0$ (day)	$m_j^0$ (mag)	$\mu_j$ (mmag day <sup>-1</sup> )	$\epsilon_j$ (mag)
Decaying phase of the 2002–2003 outburst				
V		17.50 ± 0.06	9 ± 2	0.16 ± 0.02
I	52742	16.29 ± 0.05	8 ± 2	0.14 ± 0.02
J		15.32 ± 0.09	6 ± 3	0.20 ± 0.03
H		14.80 ± 0.06	3 ± 2	0.13 ± 0.02
Rising phase of the 2004–2005 outburst				
V		16.48 ± 0.03	-4 ± 1	0.11 ± 0.01
I	53229	15.46 ± 0.03	-4 ± 1	0.11 ± 0.01
J		14.43 ± 0.07	-2 ± 1	0.17 ± 0.03
H		14.17 ± 0.06	-3 ± 1	0.11 ± 0.02
Decaying phase of the 2004–2005 outburst				
V		17.35 ± 0.06	15 ± 2	0.20 ± 0.02
I	53477	16.18 ± 0.05	13 ± 2	0.17 ± 0.02
J		15.15 ± 0.04	11 ± 1	0.14 ± 0.02
H		14.69 ± 0.04	8 ± 1	0.12 ± 0.01
Decaying phase of the 2007 outburst				
V		17.51 ± 0.06	12 ± 2	0.15 ± 0.02
I	54240	16.36 ± 0.06	11 ± 2	0.16 ± 0.02
J		15.28 ± 0.06	6 ± 2	0.14 ± 0.02
H		14.78 ± 0.09	2 ± 3	0.18 ± 0.03
Rising phase of the 2010–2011 outburst				
V		16.53 ± 0.04	-9 ± 1	0.16 ± 0.01
I	55302	15.50 ± 0.03	-10 ± 1	0.15 ± 0.01
J		14.57 ± 0.04	-8 ± 1	0.14 ± 0.01
H		14.20 ± 0.04	-7 ± 1	0.15 ± 0.01
Decaying phase of the 2010–2011 outburst				
V		17.91 ± 0.14	45 ± 10	0.21 ± 0.05
I	55606	16.68 ± 0.11	38 ± 8	0.19 ± 0.04
J		15.57 ± 0.11	32 ± 7	0.18 ± 0.04
H		15.05 ± 0.16	22 ± 11	0.22 ± 0.06

Recently, the CMD was used to study the spectral evolution of the black hole X-ray binary XTE J1550–564 during its 2000 outburst (Poutanen et al. 2014), which was very similar to that of GX 339–4. Notably, the highest SS disk temperature of 16 kK reached by XTE J1550–564 is substantially smaller than the temperature of 50 kK in GX 339–4 (see Fig. 8). The inferred SS temperatures can be affected if  $A_V$  is overestimated. We note, however, that for a lower  $A_V$  the disk temperature becomes smaller, leading to a different curvature of the blackbody track on the CMD, inconsistent with the observed shape drawn by the SS data points (see Fig. 4, solid orange line and dotted orange contour). Further, the UV observations of GX 339–4 carried out during the early phase of the 2010–2011 SS suggest that the peak of the blackbody component lies at wavelengths shorter than  $\approx 2000$  Å, beyond the near-UV (see fig. 7 in Cadolle Bel et al. 2011), which imposes a lower limit of  $\approx 15$  kK on the blackbody temperature at the beginning of the SS. Unlike XTE J1550–564, which shows a typical exponential decay of ONIR fluxes during its SS, ONIR fluxes of GX 339–4 increase shortly after the HtS transition in two out of four regular outbursts. As a result, the highest color temperatures of GX 339–4 are observed somewhere in the

middle of the SS, while the highest blackbody temperature of XTE J1550–564 is found at the beginning of the SS.

The disk temperatures depend on the flux irradiating the outer parts of the disk. This flux is defined by the disk geometry, luminosity of the central X-ray source and its emission pattern, which in turn depends on the black hole spin. The accretion disk in GX 339–4 can be a factor of  $\sim 2$  smaller than that in XTE J1550–564 (see Table 2; also Orosz et al. 2011). Geometrically thicker outer parts of the disk may also increase the amount of irradiation flux received. Then, the light bending effects in the vicinity of a Kerr black hole substantially increase the intensity of the illuminating flux (Suleimanov et al. 2008). There is evidence that the black hole spin of GX 339–4 can be as large as  $a \approx 0.935$  (Reis et al. 2008, Miller et al. 2008; but see also Kolehmainen & Done 2010; Kolehmainen et al. 2011 who give an upper limit of 0.9), compared to  $a \approx 0.5$  in XTE J1550–564 (Steiner et al. 2011). It is possible that a combination of these factors leads to a higher SS temperatures inferred in GX 339–4. Furthermore, the extinction in XTE J1550–564 assumed by Poutanen et al. (2014) might have been underestimated; a higher  $A_V$  would result in a larger temperature bringing it closer to the values measured in GX 339–4.

The Q states of GX 339–4 appear to deviate from those observed in XTE J1550–564. While for XTE J1550–564 these points lie on the blackbody track, for GX 339–4 they lie below the blackbody curve. It is known that the contribution of the companion star is small even in quiescence (up to 50 per cent to the J and H filters, Heida et al. 2017), and the red spectrum of the K-type companion cannot explain the shift towards the blue part of the CMD, as well as substantial variability of colors in GX 339–4. Other LMXBs are known to exhibit quiescent flickering, but the magnitude of quiescent variability of GX 339–4 and significant changes in observed colors exceed that measured for other sources (Zurita et al. 2003). A possible explanation for this behavior is the emission from the spiral arms, hotspots and hot line, flares triggered by the magnetic field reconnection in the vicinity of the disk, and the presence of edges and lines in the quiescent spectra (see e.g. Zurita et al. 2003; Cherepashchuk et al. 2019; Baptista & Wojcikiewicz 2020).

We find that the regular and failed outbursts occupy the same regions in the CMD. Though the regular outbursts tend to be more luminous during the RHS, the position of points of 2004–2005 outburst intersects with brightest parts of the analysed failed outbursts. We thus conclude that the peak ONIR brightness has no predictive power for the failed outbursts. The reason for the similarity of ONIR brightness of regular and failed outbursts is not clear from the light curve and CMD analysis. If the failed outbursts differ from the regular ones by the mass transfer rate, then the similar brightness during the RHS can be explained by a weak dependence of the non-thermal component on the accretion rate. Because it dominates in the ONIR, the difference between regular and faint outbursts is minor.

#### 4.2. ONIR vs X-ray correlation

Black hole LMXBs show strong non-linear correlation between radio, ONIR and X-ray fluxes. The radio–X-ray correlation was first documented for Cyg X-1, GX 339–4 and V404 Cyg (Brocksopp et al. 1999; Corbel et al. 2000; Gallo et al. 2003) and later was confirmed on a much larger sample of Galactic LMXBs (including GX 339–4 during multiple outbursts, see Corbel et al. 2013b; Islam & Zdziarski 2018). The global ONIR–X-ray correlation, which naturally arises from the different emission mechanisms (van Paradijs & McClintock 1994; Gallo et al. 2003),

**Table 6.** Best-fit parameters for model given by Eq. (7) for the hard-state radio to ONIR spectra and the soft-state ONIR spectrum of GX 339–4 shown in Fig. 14.

Dates (MJD)	Blackbody <sup>a</sup>	Hot flow <sup>b</sup>			Jet <sup>c</sup>				$N_{WISE}^d$
	$T$ ( $10^4$ K)	$N_{hf}$ (mJy)	$\nu_{hf}$ ( $10^{13}$ Hz)	$\alpha$	$N_{jet}$ (mJy)	$\nu_{jet}$ ( $10^{13}$ Hz)	$\beta$	$\gamma$	
55266.28	$3.10 \pm 0.02$	$35.5 \pm 0.2$	$1.1 \pm 0.4$	$-0.03 \pm 0.02$	$11.6 \pm 0.1$	$4.6 \pm 0.7$	$0.22 \pm 0.03$	$1.8 \pm 0.4$	$0.97 \pm 0.06$
55266.35						$0.97 \pm 0.25$			$0.74 \pm 0.02$
55266.41						$< 0.73$			$0.76 \pm 0.02$
55301.36						...			...

**Notes.** <sup>(a)</sup> Blackbody normalization was fixed at  $\log N_{bb} = 4.09$  and blackbody parameters are the same for all four spectra. <sup>(b)</sup> Hot flow parameters are the same for the three hard-state spectra. <sup>(c)</sup> Jet parameters, except cutoff frequency, are the same for the three hard-state spectra. <sup>(d)</sup> Cross-calibration factor of the *WISE* data. Errors are  $1\sigma$ .

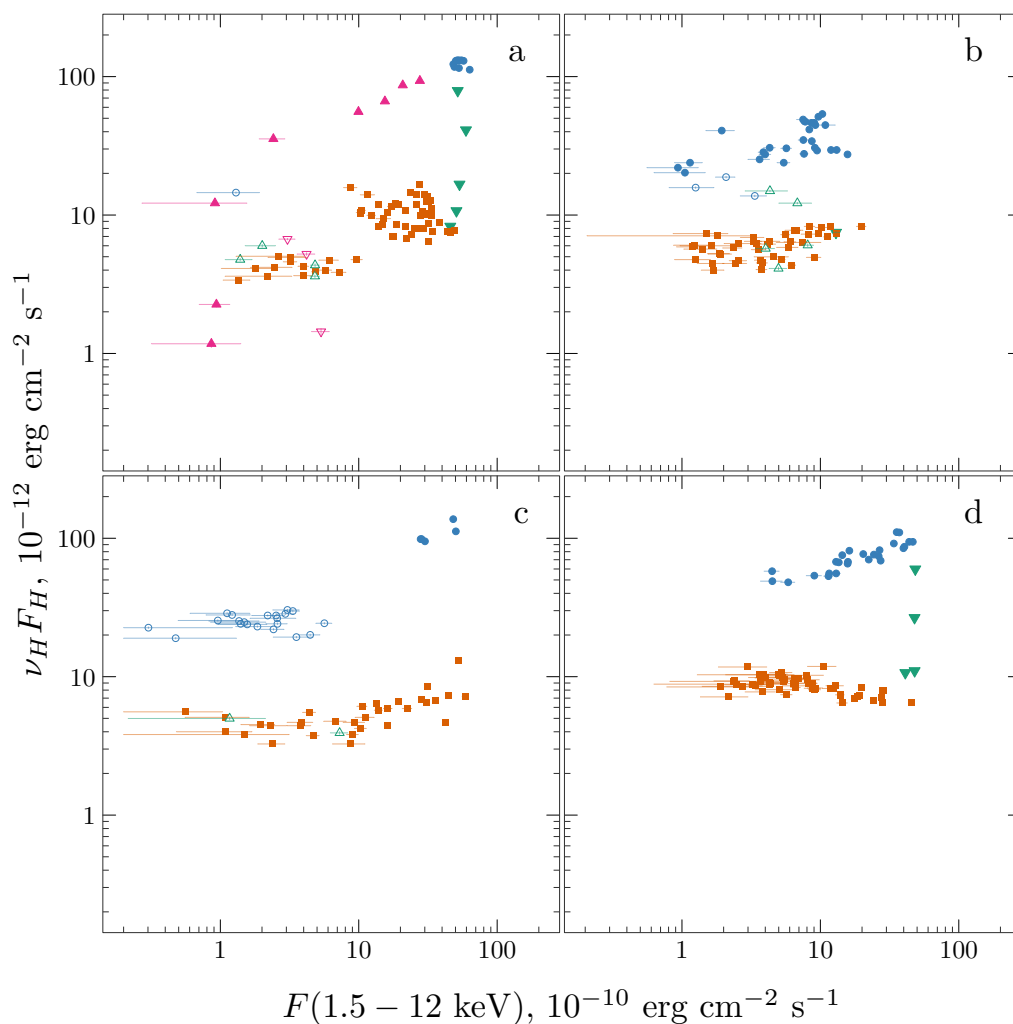


**Fig. 15.** Quasi-simultaneous ONIR  $\nu_H F_H$  versus X-ray 1.5–12 keV flux diagram. The X-ray data are taken from all three ASM bands. The colors and symbols are the same as in Fig. 5 and errors are  $1\sigma$ . (a) 2002–2003, (b) 2004–2005, (c) 2007, and (d) 2010–2011 outbursts.

was observed for a number of black hole LMXBs (Russell et al. 2006) and for the 2002–2003, 2004–2005 and 2007 outbursts of GX 339–4, in particular (see Homan et al. 2005; Coriat et al. 2009). Here we expand the sample to include the 2010–2011 outburst.

We use the *RXTE*/ASM flux as a proxy for the X-ray luminosity. The observed flux, however, cannot be simply trans-

formed into the bolometric luminosity, as the latter depends on the spectral shape. The bolometric correction is large in the hard state and the quiescence as most of the emission is radiated at energies above the ASM passband. We use the observed *H*-band flux as a proxy for the luminosity of the non-thermal component. Fig. 15 shows the relation between the *H*-band and X-ray fluxes for the regular outbursts (see also Zdziarski et al. 2002). The

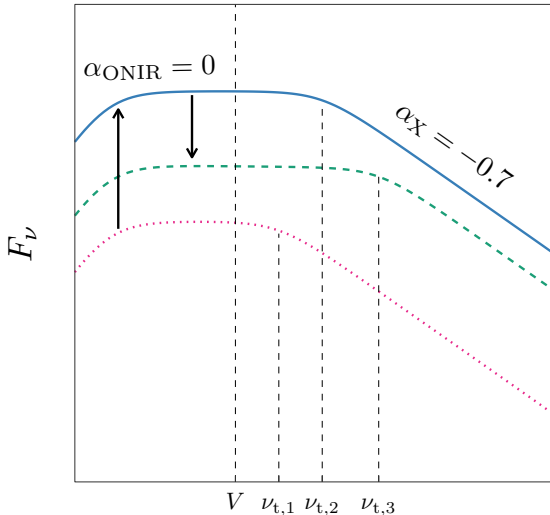


**Fig. 16.** Schematic representation of the evolution of GX 339–4 spectra during the rising phase hard state and HtS transition of an outburst. The dotted pink line is the RPh hard spectrum, the solid blue line is the RHS, and the dashed green line is HtS transition. Vertical black arrows indicate the transition sequence. Characteristic turnover frequency of each spectrum and the  $V$  filter frequency are shown with the vertical dashed lines. Characteristic spectral slopes in the ONIR and X-ray ranges are shown with  $\alpha_{\text{ONIR}}$  and  $\alpha_X$ .

source moves in the clockwise direction on this diagram with the hysteresis pattern being similar to that found by Coriat et al. (2009).

In the beginning of the SS, the  $H$ -band flux is nearly constant, with a hint of anti-correlation with the X-ray flux in the last outburst (Fig. 15d), which is likely caused by the changing bolometric correction. Such anti-correlation between ONIR and X-ray fluxes is atypical for GX 339–4 and other LMXBs, for which HS and SS correlations have very similar slopes (Fig. 15a,b,c; also Russell et al. 2006, 2007; Coriat et al. 2009). The RHS of the 2010–2011 outburst (Fig. 15d) seems to have a slope, which is not as steep as observed in other outbursts, with  $\partial \log(\nu_H F_H) / \partial \log F(\text{ASM}) \approx 0.3$ , as compared to  $\approx 0.4$  for the 2002–2003 and 2007 events.

The relation between ONIR and X-ray fluxes can be used to put constraints on the models of spectral formation in accreting black holes. The scaling of the ONIR and X-ray fluxes with the mass accretion rate was used to predict the observed ONIR – X-ray correlation in the jet-dominated scenario (Russell et al. 2006). Here we suggest an interpretation of the HS correlation in the framework of the hot accretion flow model (Veledina et al. 2013; Poutanen & Veledina 2014). The schematic representation of the spectrum in the ONIR–X-ray range is shown in Fig. 16. For a broken power-law spectrum, we can relate the ONIR ( $L_o$ ) and X-ray ( $L_x$ ) luminosities as:

$$\frac{L_o}{L_{\nu_t}} = \left( \frac{\nu_o}{\nu_t} \right)^{\alpha_{\text{ONIR}}}, \quad \frac{L_x}{L_{\nu_t}} = \left( \frac{\nu_x}{\nu_t} \right)^{\alpha_X}, \quad (8)$$

where  $\nu_t$  is the (break) turnover frequency,  $\alpha_{\text{ONIR}}$  and  $\alpha_X$  are spectral slopes and  $\nu_o$  and  $\nu_x$  are characteristic frequencies in the ONIR and X-ray ranges, respectively. The ratio of the X-ray to

ONIR luminosity is then

$$\frac{L_x}{L_o} = \left( \frac{\nu_x}{\nu_t} \right)^{\alpha_X} \left( \frac{\nu_o}{\nu_t} \right)^{-\alpha_{\text{ONIR}}} = \frac{\nu_x^{\alpha_X}}{\nu_o^{\alpha_{\text{ONIR}}}} \nu_t^{\alpha_{\text{ONIR}} - \alpha_X}. \quad (9)$$

Therefore the slope of the optical–X-ray correlation is

$$\gamma \equiv \frac{\partial \log L_o}{\partial \log L_x} = 1 - \beta (\alpha_{\text{ONIR}} - \alpha_X), \quad (10)$$

where  $\beta \equiv \partial \log \nu_t / \partial \log L_x$ .

We take  $\alpha_X \approx -0.7$  and  $\alpha_{\text{ONIR}} \approx 0$  (average of four regular outbursts, see Sect. 3 and Fig. 12). The turnover frequency scales with the magnetic field  $B$  and the Thomson optical depth  $\tau$  across the flow as

$$\nu_t \propto B^{\frac{p+2}{p+4}} \tau^{\frac{2}{p+4}}, \quad (11)$$

where  $p$  is the power-law slope of the electron distribution. Assuming density scaling with the accretion rate  $\rho \propto \dot{m}$  (i.e.  $\tau \propto \dot{m}$  too) and equipartition magnetic field  $B^2 \propto \rho$  (assuming constant temperature), we arrive at

$$\nu_t \propto \dot{m}^{\frac{p+6}{2(p+4)}}. \quad (12)$$

The bolometric luminosity scales with the accretion rate as  $\dot{m}$  or as  $\dot{m}^2$  for the cases of hot, radiatively efficient (e.g. Bisnovatyi-Kogan & Lovelace 1997) or inefficient (advection-dominated) accretion flow (e.g. Narayan & Yi 1995), respectively. For these two cases we get

$$\beta_{\text{bol}} \equiv \frac{\partial \log \nu_t}{\partial \log L_{\text{bol}}} = \frac{p+6}{2(p+4)} \quad \text{or} \quad \beta_{\text{bol}} = \frac{p+6}{4(p+4)}. \quad (13)$$

Taking  $p = 4$  to satisfy the slope of the MeV emission observed from Cyg X-1 (McConnell et al. 2002), we get  $\beta_{\text{bol}} = 0.63$  and 0.31 for the two cases. Assuming  $\beta = \beta_{\text{bol}}$  we get  $\gamma \approx 0.56$  and 0.78, respectively. This range of  $\gamma$  is consistent with the observed slope of the optical–X-ray correlation  $\gamma_{\text{obs}} \approx 0.6$  obtained in Russell et al. (2006) for a number of black hole LMXB sources. We observe  $\gamma_{\text{obs}} \approx 0.4$  (similar to  $\gamma_{\text{obs}} \approx 0.48$  in Coriat et al. 2009). Such slopes require  $\beta \approx 0.8 - 0.9$ , which is hard to achieve. However, the underestimated value of  $\gamma$  can be caused by the variable bolometric correction. If it is positively correlated with the luminosity (see Zdziarski et al. 2004; Koljonen & Russell 2019)<sup>5</sup> then

$$\beta = \beta_{\text{bol}} \frac{\partial \log L_{\text{bol}}}{\partial \log L_x} > \beta_{\text{bol}}, \quad (14)$$

bringing  $\gamma$  closer to the observed range.

#### 4.3. Origin of the non-thermal ONIR component

The nature of the red non-thermal component seen in LMXBs during the ONIR flares is debated. Two main candidates are proposed: synchrotron emission from the jet or from the hybrid hot accretion flow (see reviews by Uttley & Casella 2014; Poutanen & Veledina 2014). In some cases the ONIR soft spectrum is consistent with the optically thin synchrotron emission, and has been modeled with the jet (e.g. MAXI J1836–194; Russell et al. 2014;

<sup>5</sup> We note that bolometric correction can increase towards lower luminosities, because the rising electron temperature (Veledina et al. 2013) results in a larger fraction of flux to emerge above 200 keV as well as in the ONIR band.

Péault et al. 2019). In other cases, when the disk-subtracted non-thermal component had a hard spectrum (Poutanen et al. 2014), or when the extrapolation of the radio continuum significantly underestimates ONIR fluxes (e.g. SWIFT J1753.5–0127; Chiang et al. 2010; Kajava et al. 2016), the excess ONIR emission has been attributed to the hot accretion flow. A way to discriminate between the two models is to track the behavior of non-thermal component during the ONIR state transition. In a simple jet scenario, the spectrum from radio to optical wavelengths can be described by a broken power law (Blandford & Königl 1979), with partially-absorbed and optically thin parts. During the HtS transition the synchrotron break frequency is expected to decrease, as it scales inversely-proportional to the inner disk radius (Heinz & Sunyaev 2003). In the hot flow model, the spectrum from infrared to X-rays is expected to have two breaks: the lower-frequency break between the partially-absorbed and fully self-absorbed parts (it corresponds to the extent of the flow), and the higher-frequency break between the partially-absorbed and synchrotron Comptonization parts (Veledina et al. 2013). Under the simplest assumptions, the state transition is accompanied by the collapse of the flow outer parts, and so the lower-frequency break is expected to increase, while the spectral slope of the partially self-absorbed part can remain the same. The reverse trends are expected in the same scenarios for the StH transitions.

Unlike expected in these two simplest scenarios, we find that the non-thermal component has a constant spectral shape during the HtS and StH transitions, and only its normalization decreases (see lower panels in Fig. 12). We propose that the aforementioned evolution can be understood in terms of the hot-flow model, if both the energy release and the electron number density increase when the accretion rate increases during RPh. This then leads to the increase of total luminosity and the increase of the higher break frequency. As the accretion rate increases, the synchrotron emission, produced at the same physical radius in the flow, would shift to higher frequencies (as the frequency of self-absorption increases) and become brighter (see changes between dotted and solid lines and between turnover frequencies  $\nu_{t,1}$  and  $\nu_{t,2}$  in Fig. 16). In this model, the RHS is described by the increase of ONIR luminosity with a nearly constant spectral shape (as the latter is determined by the distribution of parameters over the radius, rather than by their absolute values). At the HtS transition, when the energy release is shifting from the hot accretion flow to the geometrically thin accretion disk, the energy deposited in the hot flow decreases, while the particle density may still increase. This results in a higher break frequency, but smaller overall ONIR luminosity (see changes between solid and dashed lines and between turnover frequencies  $\nu_{t,2}$  and  $\nu_{t,3}$  in Fig. 16).

The hot-flow model is capable of explaining both (nearly) constant colors of the non-thermal component during the RHS, as well as the constant spectral shape at decreasing ONIR luminosity during the HtS state transition if the hot flow extent during the observed transitions has not decreased. This would guarantee that the emission in the  $H$  filter appears in the partially self-absorbed part. Thus in contrast to the expectations of the original scenario the data can be described by the hot-flow model if there is no collapse of the outer parts of the flow. We suggest that the survival of the synchrotron-emitting plasma with the inwards-moving inner edge of the disk can be seen as the transition from the hot flow (within the boundaries of the cold disk) to the corona atop of the accretion disk. This scenario is supported by the StH transition and the DHS, where we observe the same evolution happening in reverse. During the StH the spectra are nearly flat and their shapes do not change (see Figs. 12a\*,c\*,d\*,f\*), indicat-

ing that the  $H$  filter remains in the self-absorbed part and we observe a reverse process of transition from the hot corona atop of the disk to the hot flow, as the inner edge of the disk moves outward.

The shape of the ONIR spectra in the simplest jet scenario depends on the break frequency, which may lie beyond the  $V$ -band ( $> 5 \times 10^{14}$  Hz, see Coriat et al. 2009; Dinçer et al. 2012; Buxton et al. 2012), or in the mid-IR ( $10^{13-14}$  Hz, see e.g. Corbel & Fender 2002; Gandhi et al. 2011). The problem is that estimates of the break frequency were obtained for different outbursts using different estimates for the extinction (see Homan et al. 2005, Maitra et al. 2009, and Buxton et al. 2012). In our interpretation of the quasi-simultaneous mid-IR data obtained with *WISE* (Gandhi et al. 2011), there is likely another highly variable soft non-thermal component, which contributes to the mid-IR in addition to the power law. GX 339–4 shows two distinct mid-IR spectral profiles: a low-flux flat one, which agrees with the power-law-like disk-subtracted ONIR spectrum, and a high-flux soft one, which drops sharply between  $W1$  and  $H$  filters (see Fig. 14). If we interpret this additional soft component as coming from the jet, the jet break frequency is about  $10^{14}$  Hz (see Table 6). This implies that the jet can dominate mid-IR fluxes, but as soon as the jet spectral slope (as determined from the radio data) changes to negative, the hot flow becomes the dominant source of the mid-IR emission, providing a baseline flux level in the mid-IR and ONIR filters. The shape and evolution of the ONIR spectra are then determined by the sum of the thermal disk and flat hot-flow components with little to no contribution from the jet.

The fast variability observed in GX 339–4 can shed more light on the nature of the ONIR emission. Within the hot-flow model, two components contribute to the variability in ONIR: synchrotron emission from the hot flow and reprocessing of the X-rays in the accretion disk. In this model (Veledina et al. 2011), a precognition dip in the optical-X-ray CCF is explained by anticorrelation of the ONIR synchrotron and the X-ray Comptonization components. The reprocessing produces a positive peak at positive lags. Together they can produce a typical CCF observed in many BH X-ray binaries (see Poutanen & Veledina 2014) including GX 339–4 (Gandhi et al. 2008, 2010). The IR/X-ray correlation, however, appears to depend on the type and phase of the outburst. The CCF obtained for the 2008 failed outburst (low-flux hard state) shows no precognition dip and only slight asymmetry (Casella et al. 2010), while CCF of the RHS of the 2010–2011 outburst features a precognition dip (Kalamkar et al. 2016). Although it is possible to explain this behavior within jet-only paradigm (see e.g. Malzac et al. 2018), it is likely that both jet and accretion flow produce different features of the IR/X-ray CCF (see also Section 3.7).

## 5. Conclusions

We analyzed the 2002–2011 ONIR light curves of GX 339–4. We used the ONIR data to separate the states of the source and compared the estimated transition dates with those obtained from the X-ray spectra. We measured the typical durations of various outburst stages: the HtS state transitions take typically a week, while the StH state transitions last twice longer. The duration of the hard state at the decaying stage is about four weeks.

Using the SS data from four regular outbursts, we determined the interstellar extinction towards the source, which allowed us to measure the intrinsic ONIR spectral slopes during different phases of the outbursts. We showed that during the outbursts the source passes through the same areas on the CMD, giving us



an opportunity to construct a template where different outburst phases are identified.

During the SS, the object is found to follow the blackbody model with a constant normalization. During the HS, a red non-thermal component dominates the  $H$  band, with the flux being higher at the rising phase than at the decaying phase. We find that the end of the HtS transitions corresponds to the blackbody temperature is 30–40 kK, while at the start of the reverse transition the temperature is  $\approx 20$  kK. In quiescence, the spectrum of GX 339–4 is bluer than the blackbody model with the same normalization, which can be explained either by the presence of strong spectral features (edges), or by the decrease of the apparent emitting area. The corresponding disk temperatures are well above the hydrogen ionization limit. The variability of the source in this state exceeds the measurements errors and its nature is uncertain.

We traced the evolutionary tracks of the failed outbursts on the CMD and found that their HS show the same colors as the HS of regular outbursts, but lower ONIR fluxes. The decay of a failed outburst follows the same track as the decaying phase of a regular outburst. These properties make it difficult to predict the failed outburst at early stages using ONIR data alone. We found that a bright RHS,  $V < 16$  mag, is a sign of a regular outburst.

Finally, we investigated the behavior of the non-thermal component, which dominates the ONIR fluxes during the HS and the state transitions. For this, we subtracted the contribution of the thermal component (disk) using the extrapolated SS light curves. We found that the luminosity of the non-thermal component evolves with a nearly constant power-law spectrum with energy spectral index  $\alpha \approx 0$  (where  $F_\nu \propto \nu^\alpha$ ). We proposed that this evolution can be explained by a model where the non-thermal component originates from the synchrotron emission of the hot accretion flow. However, for this model to work, the extent of the hot medium should not decrease at the state transitions, but instead the hot flow should transform into the hot corona atop of the accretion disk as the inner disk radius moves inward during the HtS transition. In this case, the  $H$ -filter remains in the partially self-absorbed region implying constant spectral shape. The reverse process may occur during the StH transition. Using radio ATCA and mid-IR *WISE* data contemporaneous with the available SMARTS data, we also showed that an additional strongly variable component, likely associated with the jet, is required in the mid-IR band. The spectrum of this component has a sharp cutoff below  $10^{14}$  Hz. We also detected a low-frequency cutoff in the hot flow component at  $\sim 10^{13}$  Hz, which can be used to estimate its size of about  $3 \times 10^9$  cm. We conclude that at least three components (the disk, the hot flow and the jet) are required to explain the broad-band mid-IR to ONIR spectra of GX 339–4 at different stages of its outburst.

## Acknowledgements

We thank the anonymous referees for valuable comments and suggestions, which helped improve the manuscript. AV acknowledges support from the Academy of Finland grant 309308. VFS was supported by the DFG grant WE 1312/51-1, the German Academic Exchange Service (DAAD) travel grants 57405000 and 57525212 and by the Magnus Ehrnrooth Foundation travel grant. This research was also supported by the Academy of Finland travel grants 317552 and 331951 (IAK, JP). This paper has made use of SMARTS optical/near-infrared light curves. AV thanks the International Space Science Institute (ISSI) in Bern, Switzerland for support.

## References

- Baptista, R. & Wojcikiewicz, E. 2020, *MNRAS*, 492, 1154
- Barthelmy, S. D., Barbier, L. M., Cummings, J. R., et al. 2005, *Space Sci. Rev.*, 120, 143
- Belloni, T., Homan, J., Casella, P., et al. 2005, *A&A*, 440, 207
- Belloni, T., Parolin, I., Del Santo, M., et al. 2006, *MNRAS*, 367, 1113
- Belloni, T. M. 2010, in *Lecture Notes in Physics*, Vol. 794, *The Jet Paradigm*, ed. T. Belloni (Berlin: Springer Verlag), 53
- Bisnovatyi-Kogan, G. S. & Lovelace, R. V. E. 1997, *ApJ*, 486, L43
- Blandford, R. D. & Königl, A. 1979, *ApJ*, 232, 34
- Bradt, H. V., Rothschild, R. E., & Swank, J. H. 1993, *A&AS*, 97, 355
- Brocksopp, C., Fender, R. P., Larionov, V., et al. 1999, *MNRAS*, 309, 1063
- Buxton, M. & Vennes, S. 2003, *MNRAS*, 342, 105
- Buxton, M. M. & Bailyn, C. D. 2004, *ApJ*, 615, 880
- Buxton, M. M., Bailyn, C. D., Capelo, H. L., et al. 2012, *AJ*, 143, 130
- Cadolle Bel, M., Rodriguez, J., D’Avanzo, P., et al. 2011, *A&A*, 534, A119
- Cardelli, J. A., Clayton, G. C., & Mathis, J. S. 1989, *ApJ*, 345, 245
- Casella, P., Maccarone, T. J., O’Brien, K., et al. 2010, *MNRAS*, 404, L21
- Chen, W., Shrader, C. R., & Livio, M. 1997, *ApJ*, 491, 312
- Cherepashchuk, A. M., Katysheva, N. A., Khruzina, T. S., et al. 2019, *MNRAS*, 490, 3287
- Chiang, C. Y., Done, C., Still, M., & Godet, O. 2010, *MNRAS*, 403, 1102
- Corbel, S., Aussel, H., Broderick, J. W., et al. 2013a, *MNRAS*, 431, L107
- Corbel, S., Coriat, M., Brocksopp, C., et al. 2013b, *MNRAS*, 428, 2500
- Corbel, S. & Fender, R. P. 2002, *ApJ*, 573, L35
- Coriat, M., Fender, R. P., Tzioumis, A. K., et al. 2000, *A&A*, 359, 251
- Coriat, M., Corbel, S., Buxton, M. M., et al. 2009, *MNRAS*, 400, 123
- De Marco, B., Ponti, G., Muñoz-Darias, T., & Nandra, K. 2015, *ApJ*, 814, 50
- DePoy, D. L., Atwood, B., Belville, S. R., et al. 2003, in *Society of Photo-Optical Instrumentation Engineers (SPIE) Conference Series*, Vol. 4841, *Instrument Design and Performance for Optical/Infrared Ground-based Telescopes*, ed. M. Iye & A. F. M. Moorwood, 827–838
- Dinçer, T., Kalemci, E., Buxton, M. M., et al. 2012, *ApJ*, 753, 55
- Done, C., Gierliński, M., & Kubota, A. 2007, *Astronomy and Astrophysics Review*, 15, 1
- Durant, M., Gandhi, P., Shahbaz, T., et al. 2008, *ApJ*, 682, L45
- Durant, M., Gandhi, P., Shahbaz, T., Peralta, H. H., & Dhillon, V. S. 2009, *MNRAS*, 392, 309
- Durant, M., Shahbaz, T., Gandhi, P., et al. 2011, *MNRAS*, 410, 2329
- Eggleton, P. P. 1983, *ApJ*, 268, 368
- Esin, A. A., McClintock, J. E., & Narayan, R. 1997, *ApJ*, 489, 865
- Fabian, A. C., Guilbert, P. W., Motch, C., et al. 1982, *A&A*, 111, L9
- Fender, R., Corbel, S., Tzioumis, T., et al. 1999, *ApJ*, 519, L165
- Fender, R. P. 2001, *MNRAS*, 322, 31
- Frank, J., King, A., & Raine, D. J. 2002, *Accretion Power in Astrophysics: Third Edition* (Cambridge, UK: Cambridge University Press)
- Gallo, E., Fender, R. P., & Pooley, G. G. 2003, *MNRAS*, 344, 60
- Gallo, E., Migliari, S., Markoff, S., et al. 2007, *ApJ*, 670, 600
- Gandhi, P., Blain, A. W., Russell, D. M., et al. 2011, *ApJ*, 740, L13
- Gandhi, P., Dhillon, V. S., Durant, M., et al. 2010, *MNRAS*, 407, 2166
- Gandhi, P., Makishima, K., Durant, M., et al. 2008, *MNRAS*, 390, L29
- Gehrels, N., Chincarini, G., Giommi, P., et al. 2004, *ApJ*, 611, 1005
- Gierliński, M., Zdziarski, A. A., Poutanen, J., et al. 1999, *MNRAS*, 309, 496
- Gilfanov, M. 2010, in *Lecture Notes in Physics*, Vol. 794, *The Jet Paradigm*, ed. T. Belloni (Berlin: Springer Verlag), 17–52
- Heida, M., Jonker, P. G., Torres, M. A. P., & Chiavassa, A. 2017, *ApJ*, 846, 132
- Heinz, S. & Sunyaev, R. A. 2003, *MNRAS*, 343, L59
- Homan, J. & Belloni, T. 2005, *Ap&SS*, 300, 107
- Homan, J., Buxton, M., Markoff, S., et al. 2005, *ApJ*, 624, 295
- Hynes, R. I., Haswell, C. A., Chaty, S., Shrader, C. R., & Cui, W. 2002, *MNRAS*, 331, 169
- Hynes, R. I., Haswell, C. A., Cui, W., et al. 2003a, *MNRAS*, 345, 292
- Hynes, R. I., Mauche, C. W., Haswell, C. A., et al. 2000, *ApJ*, 539, L37
- Hynes, R. I., O’Brien, K., Mullally, F., & Ashcraft, T. 2009, *MNRAS*, 399, 281
- Hynes, R. I., Steeghs, D., Casares, J., Charles, P. A., & O’Brien, K. 2003b, *ApJ*, 583, L95
- Islam, N. & Zdziarski, A. A. 2018, *MNRAS*, 481, 4513
- Jain, R. K., Bailyn, C. D., Orosz, J. A., McClintock, J. E., & Remillard, R. A. 2001, *ApJ*, 554, L181
- Kajava, J. J. E., Veledina, A., Tsygankov, S., & Neustroev, V. 2016, *A&A*, 591, A66
- Kalamkar, M., Casella, P., Uttley, P., et al. 2016, *MNRAS*, 460, 3284
- Kalemci, E., Dinçer, T., Tomsick, J. A., et al. 2013, *ApJ*, 779, 95
- Kalemci, E., Tomsick, J. A., Buxton, M. M., et al. 2005, *ApJ*, 622, 508
- Kanbach, G., Straubmeier, C., Spruit, H. C., & Belloni, T. 2001, *Nature*, 414, 180
- King, A. R. & Ritter, H. 1998, *MNRAS*, 293, L42
- Kolehmainen, M. & Done, C. 2010, *MNRAS*, 406, 2206
- Kolehmainen, M., Done, C., & Diaz Trigo, M. 2011, *MNRAS*, 416, 311

- Koljonen, K. I. I. & Russell, D. M. 2019, *ApJ*, 871, 26
- Kong, A. K. H. 2008, *The Astronomer's Telegram*, 1588, 1
- Kong, A. K. H., Kuulkers, E., Charles, P. A., & Homer, L. 2000, *MNRAS*, 312, L49
- Kosenkov, I. A. & Veledina, A. 2018, *MNRAS*, 478, 4710
- Mahmoud, R. D., Done, C., & De Marco, B. 2019, *MNRAS*, 486, 2137
- Maitra, D. & Bailyn, C. D. 2008, *ApJ*, 688, 537
- Maitra, D., Markoff, S., Brocksopp, C., et al. 2009, *MNRAS*, 398, 1638
- Malzac, J., Kalamkar, M., Vincentelli, F., et al. 2018, *MNRAS*, 480, 2054
- Markert, T. H., Canizares, C. R., Clark, G. W., et al. 1973, *ApJ*, 184, L67
- McClintock, J. E. & Remillard, R. A. 2006, in *Cambridge Astrophysics Series*, Vol. 39, *Compact stellar X-ray sources*, ed. W. H. G. Lewin & M. van der Klis, 157–213
- McConnell, M. L., Zdziarski, A. A., Bennett, K., et al. 2002, *ApJ*, 572, 984
- Miller, J. M., Reynolds, C. S., Fabian, A. C., et al. 2008, *ApJ*, 679, L113
- Motch, C., Ilovaisky, S. A., & Chevalier, C. 1982, *A&A*, 109, L1
- Motch, C., Ricketts, M. J., Page, C. G., Ilovaisky, S. A., & Chevalier, C. 1983, *A&A*, 119, 171
- Motta, S., Belloni, T., & Homan, J. 2009, *MNRAS*, 400, 1603
- Motta, S., Muñoz-Darias, T., Casella, P., Belloni, T., & Homan, J. 2011, *MNRAS*, 418, 2292
- Muñoz-Darias, T., Casares, J., & Martínez-Pais, I. G. 2008, *MNRAS*, 385, 2205
- Narayan, R. & Yi, I. 1995, *ApJ*, 452, 710
- O'Donnell, J. E. 1994, *ApJ*, 422, 158
- Orosz, J. A., Steiner, J. F., McClintock, J. E., et al. 2011, *ApJ*, 730, 75
- Paczynski, B. 1977, *ApJ*, 216, 822
- Péault, M., Malzac, J., Coriat, M., et al. 2019, *MNRAS*, 482, 2447
- Poutanen, J. & Coppi, P. S. 1998, *Physica Scripta T*, 77, 57
- Poutanen, J., Krolik, J. H., & Ryde, F. 1997, *MNRAS*, 292, L21
- Poutanen, J. & Veledina, A. 2014, *Space Sci. Rev.*, 183, 61
- Poutanen, J., Veledina, A., & Revnivtsev, M. G. 2014, *MNRAS*, 445, 3987
- Poutanen, J., Veledina, A., & Zdziarski, A. A. 2018, *A&A*, 614, A79
- Rahoui, F., Coriat, M., Corbel, S., et al. 2012, *MNRAS*, 422, 2202
- Reis, R. C., Fabian, A. C., Ross, R. R., et al. 2008, *MNRAS*, 387, 1489
- Remillard, R. A. & McClintock, J. E. 2006, *ARA&A*, 44, 49
- Russell, D. M., Altamirano, D., Lewis, F., et al. 2008, *The Astronomer's Telegram*, 1586, 1
- Russell, D. M., Fender, R. P., Hynes, R. I., et al. 2006, *MNRAS*, 371, 1334
- Russell, D. M., Maccarone, T. J., Körding, E. G., & Homan, J. 2007, *MNRAS*, 379, 1401
- Russell, D. M., Maitra, D., Dunn, R. J. H., & Fender, R. P. 2011, *MNRAS*, 416, 2311
- Russell, D. M., Russell, T. D., Miller-Jones, J. C. A., et al. 2013, *ApJ*, 768, L35
- Russell, T. D., Soria, R., Motch, C., et al. 2014, *MNRAS*, 439, 1381
- Shakura, N. I. & Sunyaev, R. A. 1973, *A&A*, 500, 33
- Shidatsu, M., Ueda, Y., Tazaki, F., et al. 2011, *PASJ*, 63, S785
- Steiner, J. F., Reis, R. C., McClintock, J. E., et al. 2011, *MNRAS*, 416, 941
- Stiele, H. & Kong, A. K. H. 2017, *ApJ*, 844, 8
- Subasavage, J. P., Bailyn, C. D., Smith, R. C., et al. 2010, in *Society of Photo-Optical Instrumentation Engineers (SPIE) Conference Series*, Vol. 7737, *Observatory Operations: Strategies, Processes, and Systems III*, 77371C
- Suleimanov, V. F., Lipunova, G. V., & Shakura, N. I. 2008, *A&A*, 491, 267
- Tavecchio, F. 2017, in *AIP Conf. Ser.*, Vol. 1792, *6th International Symposium on High Energy Gamma-Ray Astronomy*, 020007
- Tomsick, J. A., Kalemci, E., Kaaret, P., et al. 2008, *ApJ*, 680, 593
- Uttley, P. & Casella, P. 2014, *Space Sci. Rev.*, 183, 453
- van Paradijs, J. & McClintock, J. E. 1994, *A&A*, 290, 133
- Veledina, A., Poutanen, J., & Vurm, I. 2011, *ApJ*, 737, L17
- Veledina, A., Poutanen, J., & Vurm, I. 2013, *MNRAS*, 430, 3196
- Warner, B. 1995, *Cambridge Astrophysics Series*, Vol. 28, *Cataclysmic variable stars* (Cambridge, UK: Cambridge University Press)
- Wilson, W. E., Ferris, R. H., Axtens, P., et al. 2011, *MNRAS*, 416, 832
- Wright, E. L., Eisenhardt, P. R. M., Mainzer, A. K., et al. 2010, *AJ*, 140, 1868
- Zacharias, M. 2018, in *High Energy Astrophysics in Southern Africa (HEASA2018)*, 33
- Zdziarski, A. A., Gierliński, M., Mikołajewska, J., et al. 2004, *MNRAS*, 351, 791
- Zdziarski, A. A., Grove, J. E., Poutanen, J., Rao, A. R., & Vadawale, S. V. 2001, *ApJ*, 554, L45
- Zdziarski, A. A., Poutanen, J., Mikołajewska, J., et al. 1998, *MNRAS*, 301, 435
- Zdziarski, A. A., Poutanen, J., Paciesas, W. S., & Wen, L. 2002, *ApJ*, 578, 357
- Zurita, C., Casares, J., & Shahbaz, T. 2003, *ApJ*, 582, 369

## Appendix A: Separation of the states

We employ a synthetic algorithm in order to distinguish between different states of the source. We distinguish 8 different phases of an outburst (including rapid transitions between states). Each phase can be identified quite easily on either color-magnitude or light curve plots. However, it can be difficult to determine exact dates at which the transitions occur. The simultaneous analysis of four different outbursts requires an objective method to determine transition dates in all of the outbursts without human intervention.

We developed an algorithm to fit a model to the transition data. We subdivide transitions into two categories: HtS and StH transitions, which share similar S- or Z-shaped profile, and the transitions to/from quiescence. The evolution of the ONIR fluxes of GX 339–4 in the vicinity of the HtS and StH can usually be well approximated by an exponential rise or decay, which corresponds to a linear trend in magnitudes. A simple sigmoid function fits two different linear trends before and after the transition and matches the intermediate S-shaped evolution:

$$S(t) = \frac{m_1 + \mu_1 \left(\frac{t-t_0}{T}\right)}{1 + \exp\left(\frac{t-t_0}{T}\right)} + \frac{m_2 + \mu_2 \left(\frac{t-t_0}{T}\right)}{1 + \exp\left(-\frac{t-t_0}{T}\right)}, \quad (\text{A.1})$$

where  $m_1, \mu_1, m_2, \mu_2$  are parameters of the linear functions,  $t_0$  is a turnover point, at which  $S(t_0) = 1/2(m_1 + m_2)$ , and  $T$  is the characteristic timescale of the transition. We then fit this model to the HtS and StH transitions using the data from the  $H$  filter light curve. The reason we chose the  $H$  filter is that the non-thermal component contributes more to this filter, making it easier to determine the turnover points.

As a result, the transition boundaries can be universally expressed in terms of  $t_0$  and  $T$ . We define HtS start date as  $t_0 - 2T$  and end date as  $t_0 + 3T$ . Similarly, for the StH transition the start date is  $t_0 - 3T$  and the end date is  $t_0 + 2T$ . The choice of the offset factors is influenced by the slopes of the trends before and after the transition. For example, at  $t = t_0 - 3T$  the contributions of the first and second trends are 5 and 95%, respectively, while at  $t = t_0 - 2T$  the trends contribute 12 and 88%, respectively. As a result of such choice, the duration of the StH or HtS transitions is  $5T$  and can be directly obtained from the fitted model parameters. An example of such outburst separation is shown in Fig. A.1(a).

The boundaries between the decaying phase and the quiescence were determined in a similar manner. Due to the differences in the quiescent state baseline fluxes between outbursts, there is no common lower limit applicable to all of the outbursts simultaneously, which can be used to determine the end of the decay. Therefore, we fit similar model to the decaying phase and quiescence data, for which we fix the parameter  $T$  at  $\frac{1}{3}$  d, corresponding to the very rapid change of the fitted model from one trend to another. We then use the turnover point  $t_0$  as a formal definition of the boundary between transition and quiescence (see Fig. A.1b, dotted blue line).

Our algorithm was also applied to the failed outbursts. We fitted our model to the 2006 and 2009 events and adopted  $t_0 - 2T$  and  $t_0 + 2T$  as the transition boundaries. For the 2008 failed outburst, we used the turnover points  $t_0$  to subdivide the light curve into 4 parts. During this event GX 339–4 showed extremely erratic behavior with no clear manifestations of the non-thermal component, therefore the phase separation is rather arbitrary and is only required for comparison to other failed outbursts.

In order to compare the decaying phase of the failed and regular outbursts, we split the interval between the end of the SS

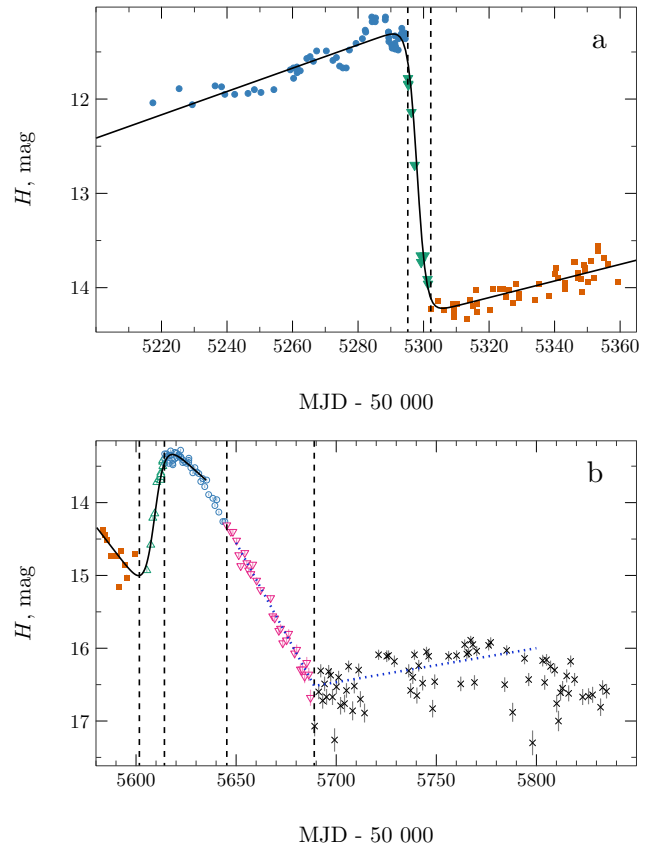


**Fig. A.1.** Example of the phase separation during (a) rise and (b) decay of the 2010–2011 outburst. Colors and symbols are same as in Fig. 4. The solid black line and dotted blue line (panel b) show the fitted models given by Eq. (A.1). Vertical dashed lines correspond to the boundaries between different phases.

and the beginning of the quiescence in half and mark the second half as DPh (see Fig. A.1b, pink open triangles). We also apply the algorithm to the rising phase of the 2002–2003 outburst, obtaining the starting date of the RPh.

Our algorithm is similar to the one used by Buxton & Bailyn (2004) and is relatively insensitive to the data selection effects, as we eliminate the process of by-eye separation of data into groups prior to fitting (Kalemci et al. 2013). As a result, this method can be used to study and compare transition dates of the outbursts observed in other LMXB transients.